

# ON THE DETERMINATION OF N AND O ABUNDANCES IN LOW METALLICITY SYSTEMS

Aida Nava, Darrin Casebeer, Richard B. C. Henry, and Darko Jevremovic

*Homer L. Dodge Department of Physics and Astronomy, The University of Oklahoma, 440  
West Brooks, Room 131, Norman OK, 73019-2061*

nava,casebeer,henry,djc@nhn.ou.edu

## ABSTRACT

We show that in order to minimize the uncertainties in the N and O abundances of low mass, low metallicity ( $O/H \leq \text{solar}/5$ ) emission-line galaxies, it is necessary to employ separate parameterizations for inferring  $T_e(N^+)$  and  $T_e(O^+)$  from  $T_e(O^{+2})$ . In addition, we show that for the above systems, the ionization correction factor (ICF) for obtaining N/O from  $N^+/O^+$ , where the latter is derived from optical emission-line flux ratios, is  $\langle ICF \rangle = 1.08 \pm 0.09$ . These findings are based on state-of-the-art single-star H II region simulations, employing our own modeled stellar spectra as input. Our models offer the advantage of having matching stellar and nebular abundances. In addition, they have O/H as low as solar/50 (lower than any past work), as well as  $\log(N/O)$  and  $\log(C/O)$  fixed at characteristic values of -1.46 and -0.7, respectively. The above results were used to re-derive N and O abundances for a sample of 68 systems with  $12 + \log(O/H) \leq 8.1$ , whose de-reddened emission-line strengths were collected from the literature. The analysis of the  $\log(N/O)$  versus  $12 + \log(O/H)$  diagram of the above systems shows the following: (1) the largest group of objects forms the well-known N/O plateau with a value for the mean (and its statistical error) of -1.43 (+.0084/-.0085); (2) the objects are distributed within a range in  $\log(N/O)$  of -1.54 to -1.27 in Gaussian fashion around the mean with a standard deviation of  $\sigma = +.071/-.084$ ; and (3) a  $\chi$ -square analysis suggests that only a small amount of the observed scatter in  $\log(N/O)$  is intrinsic.

*Subject headings:* galaxies: abundances — galaxies: evolution — galaxies: irregular—  
HII regions

## 1. INTRODUCTION

Low metallicity systems (or metal-poor systems) are low mass emission-line galaxies with  $12 + \log(\text{O}/\text{H})$  roughly in the range 7.2-8.1, where O/H is the oxygen to hydrogen number density ratio. They are referred to in the literature as dwarf irregular galaxies (dIs), their bursting derivatives, blue compact galaxies (BCGs), or H II galaxies, a subclass of BCGs dominated in the optical by H II region-like spectra (see Kunth & Östlin 2000). We use oxygen as a measure of metallicity in the above systems because it is the most abundant metal in the interstellar medium (ISM), and because its abundance can be easily determined from the emission-lines present in their optical spectra. Note that if we adopt  $12 + \log(\text{O}/\text{H})_{\odot} = 8.66 \pm 0.05$  for the solar value (Asplund 2004), then low metallicity systems have O/H in the range solar/30-solar/4. The lower limit corresponds to the value of I Zw 18, which is the most metal-poor dwarf galaxy ever observed. The upper limit ensures that the most metal rich objects are still below the onset of the observed N/O increase with O/H. In addition, objects with  $12 + \log(\text{O}/\text{H})$  below 8.1 have sufficient strength in the auroral line [O III]  $\lambda 4363$ , which is necessary in order to determine the electron temperatures required to obtain N/O.

In the  $\log(\text{N}/\text{O})$  versus  $12 + \log(\text{O}/\text{H})$  diagram (e.g., Fig. 2 of Pilyugin et al. 2004), low metallicity systems form what is known as the primary N/O plateau. For these objects, N/O is independent of O/H as is expected for the ratio of two primary elements<sup>1</sup>. The analysis of the properties of this plateau plays an important role in understanding the process of primary nitrogen production, which is essential for determining the stellar mass range most responsible for N-production, constraining stellar N-yields (in particular for massive stars), obtaining information about the initial mass function (IMF) of galaxies, and perfecting galactic chemical evolution models. Note that although one could think of other candidates for studying N/O at low metallicities, such as stars in metal-poor globular clusters, Galactic halo stars, or damped Ly $\alpha$  systems, which are quasar radiation absorbers with O/H  $\sim$  solar/10, it is much harder to measure N and O abundances in such systems. This explains why the bulk of the N/O data are from low metallicity systems.

There is disagreement among authors on the vertical thickness of the plateau and on the origin of its properties. Pagel (1985) called attention to the large scatter in N/O at fixed O/H. However, Thuan et al. (1995), Izotov et al. (1999), and Izotov et al. (2001), found that the plateau is narrow, with a dispersion of only  $\pm 0.02$  dex in  $\log(\text{N}/\text{O})$ , for objects with  $12 + \log(\text{O}/\text{H}) \leq 7.6$ . In addition, the latter authors explained the plateau in terms of

---

<sup>1</sup>An element is referred to as primary if its production process is independent of the initial metallicity of the progenitor star.

primary nitrogen from rapidly evolving massive stars ( $M > 8 M_{\odot}$ ). In contrast, Henry et al. (2000) and Chiappini et al. (2003) concluded that these objects are dominated by primary nitrogen from intermediate mass stars, which have masses in the range 4-8  $M_{\odot}$  and evolve much slower.

In order to correctly interpret the plateau properties, it is important to up-date the techniques employed to determine the N/O values. This can be accomplished through modeling. In particular, simulations are required to obtain N/O for two reasons.

Firstly, they are necessary for finding parameterizations for the electron temperatures of the regions where  $N^+$  and  $O^+$  are emitting, i.e.,  $T_e(N^+)$  and  $T_e(O^+)$ . Unfortunately, because the strengths of the auroral features [N II]  $\lambda 5755$  and [O II]  $\lambda\lambda 7320, 7230$  are commonly unavailable in observational data, the above temperatures cannot be obtained from emission-line flux ratios of the form, nebular line(s) / auroral line(s), although they are required in order to determine the abundances of the above two ions. Since photoionization models can provide the auroral lines missing from observations, these lines can be used in turn to compute  $T_e(N^+)$ ,  $T_e(O^+)$ , and  $T_e(O^{+2})$ , independent of each other. Because objects with oxygen abundances below 8.1 usually have sufficient strength in the auroral line [O III]  $\lambda 4363$ ,  $T_e(O^{+2})$  can be directly determined from the observed temperature sensitive line flux ratio  $(I_{4959} + I_{5007})/I_{4363}$  (Shields et al. 1981). In general, a parameterization of the form  $T_e(N^+) = T_e(O^+) = f[T_e(O^{+2})]$ , inferred from models, is used to compute N/O at low O/H (e.g., Kobulnicky & Skillman 1996; Izotov et al. 1999; Melbourne et al. 2004). Examples of this type of relation, based on photoionization models by Stasińska (1990), can be found in Pagel et al. (1992) or Izotov et al. (1994). A more recent parameterization based on models by Stasińska & Leitherer (1996) is used in Stasińska & Izotov (2003), although the stellar spectra used as input to these models reflect the state-of-the-art in 1995. In addition, the lowest stellar atmosphere metallicity that they used is solar/10. Ever since, more complete synthetic stellar spectra have been published for metallicities as low as solar/20 (e.g., Smith et al. 2002). Parameterizations of the form  $T_e(N^+) = f_1[T_e(O^{+2})]$  and  $T_e(O^+) = f_2[T_e(O^{+2})]$  for systems with metallicities as low as that of I Zw 18 should be obtained and compared to each other, using results from up-to-date stellar and nebular models.

Secondly, models are required for finding the ionization correction factor (ICF) necessary for obtaining N/O from  $N^+/O^+$ . Based on simulations described in Garnett & Shields (1987), which make use of Mihalas (1972) and Kurucz (1975, 1979) stellar atmospheres with effective temperatures ranging from 38 kK to 55 kK, Garnett (1990) showed that  $0.8 \lesssim (N/O)/(N^+/O^+) \lesssim 1.0$  in ionized nebulae with one-tenth (Anders & Grevesse 1989) solar abundances. More recently, Izotov et al. (2004) confirmed that  $N/O \approx N^+/O^+$  is a reasonable approximation in metal-poor H II galaxies. They established this using photoionization

models of Stasińska & Izotov (2003) with input stellar spectra generated with the stellar atmosphere code *CoStar* (Schaerer & de Koter 1997), as well as simulations computed with the evolutionary synthesis code *Starburst99* (Leitherer et al. 1999), using Smith et al. (2002) stellar spectra generated with *WM-Basic* (Pauldrach et al. 2001). Note that the spectra of Smith et al. (2002) are available for metallicities down to  $Z_{\odot}/20$ . Unfortunately, the uncertainty in the ICF is not given in Izotov et al. (2004), however, the value of the ICF is sensitive to the ionization parameter<sup>2</sup>. This parameter is a poorly constrained variable (e.g.,  $\log(U)$  ranges from -5 to -1 in models by Garnett 1989). Note that more recently, Stasińska & Leitherer (1996) found that only a small range for  $U$  can fit the emission-line diagnostics from the few H II galaxies that they modeled. However, as these authors conclude,  $U$  is yet to be observationally constrained. In addition, the value of the ICF also depends on the method employed to compute  $N^+/O^+$ . In particular, if the latter is derived from optical line flux ratios, the ICF will depend on the temperatures used to derive the  $N^+/H^+$  and  $O^+/H^+$  ratios.

Our goal is to re-derive N and O abundances for a carefully selected sample of 68 low-metallicity systems whose de-reddened optical emission-line strengths were taken from the literature (Campbell et al. 1986; Walsh & Roy 1989; Pagel et al. 1992; Skillman & Kennicutt 1993; Izotov et al. 1994; Thuan et al. 1995; Kobulnicky & Skillman 1996; Izotov et al. 1997; Kobulnicky & Skillman 1998; Izotov & Thuan 1998a,b; Izotov et al. 1999; Melbourne et al. 2004). This was accomplished using independent temperature parameterizations for  $T_e(N^+)$  and  $T_e(O^+)$  (which diverge at low metallicities, see below) and applying an ICF for obtaining N/O from  $N^+/O^+$ . Our temperature parameterizations and ICF are based on results from a representative grid of photoionization models computed with the code CLOUDY version 96.01 (Ferland et al. 1998). These employ state-of-the-art modeled stellar spectra that we generated with PHOENIX version 13.08.04A (Hauschildt & Baron 1999, 2004; Aufdenberg et al. 2002). The purpose of our work is to carefully study the morphology of the N/O plateau, assess the uncertainties, and then quantify the amount of natural scatter among plateau objects.

We discuss our general procedure for deriving the number density ratios O/H and N/O from optical emission-lines in § 2.1. In § 2.2 we describe our models and explain how we obtained the electron temperatures, electron density, and ICF relevant to the above abundance determinations. Our method for determining abundance uncertainties is explained in § 3, in which we also compare our abundances with literature results. In section § 4 we analyze the

---

<sup>2</sup>The ionization parameter can be defined as  $U \equiv Q(H) / [4 \pi r_o^2 n(H) c]$ , where,  $r_o$  is the distance from the ionizing source to the illuminated face of the cloud,  $n(H)$  is the total hydrogen density,  $c$  is the speed of light, and  $Q(H)$  is the stellar emission rate of hydrogen ionizing photons (Ferland et al. 1998).

scatter in the N/O plateau. Finally, section 5 gives a summary of our work. In a companion paper to this one (Henry et al. 2006), chemical evolution models are combined with Monte Carlo techniques to further interpret the plateau morphology.

## 2. METHOD

### 2.1. General Procedure

The N and O ionic abundances for our sample of low metallicity systems were determined directly from published optical emission-lines using the general expression:

$$\frac{X^i}{H^+} = \frac{I_\lambda}{I_{H\beta}} \frac{N_e \alpha_{H\beta}^{eff}(T_e)}{\chi^u(T_e, N_e) A_l^u} \frac{\lambda}{4861}, \quad (1)$$

where the fraction on the left is the number density ratio of the N or O ion relative to  $H^+$ , the first fraction on the right is the line flux ratio of a nebular forbidden feature of ion  $X^i$  relative to the strength of  $H\beta$ ,  $N_e$  is the electron density ( $\text{cm}^{-3}$ ),  $T_e$  is the electron temperature of the region where the relevant ion is emitting (K),  $\alpha_{H\beta}^{eff}$  is the effective recombination coefficient of  $H\beta$  which includes radiative and three-body processes ( $\text{cm}^3 \text{s}^{-1}$ ),  $\chi^u$  is the fraction of ions  $X^i$  with an electron in the upper level of the transition of interest,  $A_l^u$  is the corresponding spontaneous de-excitation rate coefficient ( $\text{s}^{-1}$ ), and the last term is the wavelength ratio of the line of interest and  $H\beta$  ( $\text{\AA}$ ). Note that equation (1) is based on the assumption that  $H\beta$  arises from recombination. The contribution to H lines from collisional excitation was neglected because the excitation potentials of H levels are much higher than the average thermal equilibrium temperature that characterizes H II regions (Osterbrock, D. E. & Ferland, G. J. 2006). In addition, equation (1) assumes that nebular forbidden lines originate from collisionally excited levels. Collisional excitation is significant in this case because the low-lying energy levels of the relevant ions are of the order of  $kT$ . However, according to Rubin (1986), recombinations of  $O^{+2}$  can excite the nebular doublet [O II]  $\lambda\lambda 3726, 3729$ , used to compute  $O^+/H^+$ . The effect of this process will be analyzed in the future.

Although the presence of the nebular He II 4686  $\text{\AA}$  emission-line in the spectra of several metal-poor systems implies the presence of unobserved  $O^{+3}/H^+$ , the contribution of this ion to the total oxygen abundance amounts to only a few percent according to our photoionization models. Therefore, we obtained the oxygen abundance by assuming that  $O/H = (O^+ + O^{+2}) / H^+$ . The N/O ratio was determined from  $N/O = \text{ICF} \times N^+/O^+$ , where the ICF was derived using models as explained in § 2.2.

A 5<sup>th</sup> order fit to data from Storey, P. J. and Hummer, D. G. (1995) was adopted for  $\alpha_{H\beta}^{eff}$ , i.e.,  $\alpha_{H\beta}^{eff} = 10^\xi$ , where  $\xi = \sum_{i=0}^5 a_i T_e^i$ . The parameters are:  $a_0 = -12.404592$ ,  $a_1 = -3.47193796 \times 10^{-4}$ ,  $a_2 = 4.98365006 \times 10^{-8}$ ,  $a_3 = -3.77545451 \times 10^{-12}$ ,  $a_4 = 1.33944026 \times 10^{-16}$ , and  $a_5 = -1.75120267 \times 10^{-21}$ . The fraction  $\chi^u$  was determined using a 5-level atom routine written and tested thoroughly for accuracy by one of us (A. N.). The equilibrium equations for each electronic level were solved using Gauss-Jordan elimination and the maximum pivot technique (Chapman 1998). Column (1) of Table 1 shows the list of ions involved in the determination of N/O. Columns (2), (3), and (4) of the same table give references for the energy levels, transition rates, and collisional strengths, respectively, employed in the 5-level atom calculations. Note that S<sup>+</sup> is included in Table 1 since  $N_e$ ([S II]) was employed in our calculations as explained in the next section.

## 2.2. Electron Temperatures, Density, and ICF

### 2.2.1. Electron Temperatures

In equation (1), three parameters,  $\alpha_{H\beta}^{eff}$ ,  $\chi^u$ , and  $N_e$ , depend on  $T_e$ . In theory,  $T_e(\text{N}^+)$ ,  $T_e(\text{O}^+)$ , and  $T_e(\text{O}^{+2})$  can be obtained from the  $T_e$  sensitive line flux ratios,  $R[\text{N II}] \equiv (I_{6548} + I_{6583})/I_{5755}$ ,  $R[\text{O II}] \equiv (I_{3726} + I_{3729})/(I_{7320} + I_{7230})$ , and  $R[\text{O III}] \equiv (I_{4959} + I_{5007})/I_{4363}$ , respectively (Shields et al. 1981). Unfortunately, in practice  $T_e(\text{N}^+)$  and  $T_e(\text{O}^+)$  cannot be directly inferred from their corresponding ratios because the auroral line [N II]  $\lambda 5755$  and the auroral doublet [O II]  $\lambda \lambda 7320, 7230$  are usually absent in observational data. However, photoionization models can predict the auroral line strengths required for deriving theoretical relations of the form  $T_e(\text{N}^+) = f_1[T_e(\text{O}^{+2})]$  and  $T_e(\text{O}^+) = f_2[T_e(\text{O}^{+2})]$ . The independent variable of these relations is  $T_e(\text{O}^{+2})$ , since this temperature can be inferred directly from the observed  $R[\text{O III}]$  ratio of low metallicity systems as long as [O III]  $\lambda 4363$  is detected with good S/N. Note that the advantage of finding individual parameterizations for  $T_e(\text{N}^+)$  and  $T_e(\text{O}^+)$  is that this minimizes the uncertainty in  $\text{N}^+/\text{O}^+$  (and N/O) which is introduced by assuming that  $T_e(\text{N}^+)$  and  $T_e(\text{O}^+)$  are equivalent functions of  $T_e(\text{O}^{+2})$ , as discussed in § 1.

In order to find separate temperature parameterizations for  $T_e(\text{N}^+)$  and  $T_e(\text{O}^+)$ , determine the ICF for obtaining N/O from  $\text{N}^+/\text{O}^+$ , and carefully estimate uncertainties in N/O, we computed a grid of photoionization models, representative of low metallicity systems. In the following paragraphs, we introduce PHOENIX, the stellar atmosphere code used to generate the spectra that served as input to our CLOUDY photoionization models, we explain the choice of parameter space covered by our stellar and nebular simulations, we describe how we proceeded to obtain the temperature parameterizations and ICF from our models, and we derive the electron temperatures, electron densities, and ionic abundances of our

sample objects.

PHOENIX is a general stellar atmosphere code which operates in one-dimensional spherically symmetric or plane-parallel geometry. It can handle static atmospheres (e.g. stars, Jupiter-like planets, brown dwarfs) as well as moving atmospheres (supernovae, novae, massive hot stars, etc.). The code simultaneously solves the equations of radiative transfer (in the proper geometry), structure, and level population in Non-Local Thermodynamic Equilibrium (NLTE).

We used PHOENIX’s wind module package (Aufdenberg et al. 2002) to generate synthetic spectra in the range from 100 to  $8 \times 10^6$  Å, for six windy O-dwarf stars with solar/5, solar/20, or solar/50 metal abundances, except for N and C, which we scaled in order to be consistent with typical proportions found in low metallicity systems, i.e.,  $\log(\text{N/O}) = -1.46$  and  $\log(\text{C/O}) = -0.7$  (Henry et al. 2000). The set of solar abundances was modified in order to match that of the code we used for our photoionization models<sup>3</sup>. Other input parameters to the models were based on those employed by Smith et al. (2002), who generated *WM-Basic* synthetic spectra for the same type of stars, with solar/5 and solar/20 proportions for all metals (including N and C).

We adopted a  $\beta$ -law for the wind velocity, i.e.,

$$v(r) = v_{\infty} (1 - R_*/r)^{\beta}, \quad (2)$$

where  $r$  is the distance from the center of the star,  $R_*$  is the radius of the “photosphere” (considered to be the base of the wind), and  $v_{\infty}$  is the terminal velocity, assumed to be reached at  $100 \times R_*$ . The  $\beta$ -index was assumed to be 0.8 (Lamers & Cassinelli 1999). The density structure in the dynamic region ( $v(r) > 0$ ) was calculated from the continuity equation:

$$\rho(r) = \frac{\dot{M}}{4 \pi r^2 v(r)}, \quad (3)$$

where,  $\rho(r)$  is the mass density and  $\dot{M}$  is the mass loss rate. In the hydrostatic region ( $v(r) = 0$ ) the density structure was calculated assuming hydrostatic equilibrium. All models have 45 zones for the dynamic region and five zones for the hydrostatic region.

A great deal of acceleration comes from resonance line radiation pressure of metals. Therefore, as in Smith et al. (2002), the dependences of  $v_{\infty}$  and  $\dot{M}$  on the metallicity were parametrized by:

$$v_{\infty} = v_{\infty, \odot} Z^{0.13}, \quad (4)$$

---

<sup>3</sup>Our software uses solar abundances by Allende Prieto et al. (2001).

and

$$\dot{M} = \dot{M}_{\odot} Z^{0.8}. \quad (5)$$

Values for  $v_{\infty, \odot}$  and  $\dot{M}_{\odot}$  can be found in Smith et al. (2002). A summary of the parameters characterizing our PHOENIX models is given in Table 2. For each model listed in column (1), columns (2) through (8) show the following information: (2) atmosphere’s metallicity, (3) stellar mass loss rate, (4) wind’s terminal velocity, (5) photospheric temperature, (6) surface gravity, (7) stellar radius, and (8) total luminosity in the range specified within parenthesis. In Figure 1, we display the ionizing portion of PHOENIX (solid lines) and *WM-Basic* (dashed lines) spectra for two solar/20 O-dwarfs. The effective temperatures of the stars are 43 kK (top panel) and 50 kK (bottom panel). Note that the PHOENIX models differ from the *WM-Basic* models in that the former have more hydrogen ionizing photons and fewer helium ionizing photons. This is due to the fact that PHOENIX absorbs the He ionizing flux due to the presence of more lines. Therefore, the normalized luminosity is re-distributed towards H ionizing energies.

We used CLOUDY to simulate the spectra of 24 single-star H II regions. The PHOENIX star used as input to each model is listed in column (1) of Table 3. Note that we reduced the spectral resolution of the PHOENIX energy distributions in order to fit CLOUDY’s default resolution. This was done using the CONGRID routine implemented in IDL version 5.5<sup>4</sup>.

The following general characteristics are shared by all of our models: spherical geometry (ionizing source fully covered), constant H density  $n(H)$ , homogeneous distribution of the gas (filling factor of 1), and static configuration. Studying the effects of using more complex models falls beyond the scope of this paper.

All nebulae have He/H = 0.1 and metal abundances identical to those of the atmospheres of the illuminating stars, except for the refractory elements Na, Mg, Al, Si, Ca and Fe, which are depleted by a factor of 10 since they are likely to be found in the form of grains in H II regions (Savage & Sembach 1996). Accordingly, grains were included in our simulations by turning on the “grains ISM” feature implemented in CLOUDY, with their abundances scaled down by a factor of 1/5, 1/20, or 1/50, in order to be consistent with the oxygen depletion of the model<sup>5</sup>.

In order to study the effect of varying the nebula’s electron density, we ran models

---

<sup>4</sup>This Solaris sunos sparc data analysis software was developed by Research Systems Inc. (2001).

<sup>5</sup>Note that CLOUDY’s ISM grains are based on an older set of solar abundances than the set used by the code to scale the H II region abundances. The latter set is based on the abundances given by Grevesse & Sauval (1998), Holweger (2001), and Allende Prieto et al. (2001, 2002)



for two different values of  $n(H)$ , 10 or 100  $\text{cm}^{-3}$ , which are typical values measured in low metallicity systems. We also varied the distance from the star to the illuminated face of the cloud ( $r_0$ ), adopting either 2 pc, (which is bigger than the radius of a planetary nebula) or 5 pc (which allowed us to cover a range for the ionization parameter comparable to what is found in the literature). The above choices resulted in  $-3.17 \leq \log(U) \leq -0.42$ . The parameters characterizing our CLOUDY models are summarized in Table 3, which gives O/H in column (2), the H density in column (3),  $r_0$  in column (4),  $\log(U)$  in column (5) and the nebular geometry in column (6). Note that the latter is plane-parallel if  $\Delta r/r_o < 0.1$ , a thick shell if  $0.1 < \Delta r/r_o < 3$ , and spherical if  $\Delta r/r_o \geq 3$ , where  $\Delta r$  is the thickness of the cloud set by the stopping temperature, chosen to be 100 K.

In order to find parameterizations of  $T_e(\text{N}^+)$  and  $T_e(\text{O}^+)$  with respect to  $T_e(\text{O}^{+2})$ , from models,  $T_e(\text{N}^+)$ ,  $T_e(\text{O}^+)$ , and  $T_e(\text{O}^{+2})$  need to be determined independent of each other first. This can be accomplished using two different methods. The first method, corresponding to common practice (Garnett 1990; Stasińska 1990; Stasińska & Leitherer 1996; Stasińska & Izotov 2003), is to compute each temperature from:

$$\langle T_e(A^{+j}) \rangle = \frac{\int T_e(A^{+j}) N_e N(A^{+j}) dV}{\int N_e N(A^{+j}) dV}, \quad (6)$$

i.e., each temperature is an ion and  $N_e$  weighted volume  $T_e$  mean. However, the above three temperatures can also be obtained from their respective line flux ratios,  $R[\text{N II}]$ ,  $R[\text{O II}]$ , or  $R[\text{O III}]$ , as explained below. This second method has the advantage of being consistent with the observational way of obtaining  $T_e(\text{O}^{+2})$ , i.e., from line flux ratios. Ideally, temperature parameterizations should be independent of the method employed to compute the individual temperatures. We will compare temperatures computed with different methods further on, but first, we will explain how we determined  $T_e(\text{N}^+)$ ,  $T_e(\text{O}^+)$ , and  $T_e(\text{O}^{+2})$  from their respective line flux ratios.

In order to accomplish the latter, we used an iterative procedure based on Brent's method for finding roots (Press et al. 1996). For each of the 24 photoionization models, the idea is to use our 5-level atom routine to compute repeatedly the theoretical line flux ratio,  $R_{the}$ , for assumed values of  $T_e$  over a range of 4-25 kK until it matches the model-predicted value  $R_{mod}$  to within a tolerance of 0.001. We carried out this procedure separately for the two density regimes of 10 and 100  $\text{cm}^{-3}$ . Using a maximum of 100 iterations to solve the equation numerically, we searched for the value of  $T_e$  which satisfied the relation:

$$\frac{R_{the}[T_e, N_e] - R_{mod}}{R_{the}[T_e, N_e]} = 0.001. \quad (7)$$

Henceforth, we will refer to models with  $n(H) = 10 \text{ cm}^{-3}$  and  $n(H) = 100 \text{ cm}^{-3}$  as the n10 and n100 models, respectively. Our temperature parameterizations for the n10 models

are

$$T_e(N^+) = -5950 + 2.256 \times T_e(O^{+2}) - 6.28 \times 10^{-5} \times T_e(O^{+2})^2 \quad (8)$$

and

$$T_e(O^+) = -5470 + 2.131 \times T_e(O^{+2}) - 5.54 \times 10^{-5} \times T_e(O^{+2})^2, \quad (9)$$

while for the n100 models they are

$$T_e(N^+) = -7720 + 2.438 \times T_e(O^{+2}) - 6.56 \times 10^{-5} \times T_e(O^{+2})^2, \quad (10)$$

and

$$T_e(O^+) = -7330 + 2.325 \times T_e(O^{+2}) - 5.82 \times 10^{-5} \times T_e(O^{+2})^2. \quad (11)$$

For each model, Figure 2 shows two independent values of  $T_e(O^{+2})$  on left panel, and two independent values of  $T_e(O^+)$  on the right panel. On the left panel, the value obtained using  $R[\text{O III}]$  is given vertically, while the value  $\langle T_e(O^{+2}) \rangle$  predicted by equation (6) is given horizontally. The agreement between the two  $T_e(O^{+2})$  temperatures is excellent. On the right panel, the parameterized  $T_e(O^+)$  given by either equation (9) or (11) [depending on the input value of  $n(H)$ ] is given vertically, with open circles representing n10 models and filled circles representing n100 models. On the same panel, the horizontal value is that predicted by equation (6). The agreement between the two  $T_e(O^+)$  temperatures is reasonable, with the parameterized value being higher than  $\langle T_e(O^+) \rangle$  for most models. The biggest difference found is  $T_e(O^+) - \langle T_e(O^+) \rangle$  of about 800 K. The effect of this difference on the  $N^+/O^+$  ratios is discussed below. Since unfortunately CLOUDY does not print out  $\langle T_e(N^+) \rangle$ , the latter temperature was not compared to the parameterized  $T_e(N^+)$ .

Figure 3 features  $T_e(N^+)$  vs.  $T_e(O^{+2})$  (top panel) and  $T_e(O^+)$  vs.  $T_e(O^{+2})$  (bottom panel), where results for the n10 and n100 models are shown with open and filled circles, respectively. In this figure, the solid lines are best fits to models sharing the same value of  $n(H)$  while the dotted lines are extrapolations to low metallicities of parameterizations of the form  $T_e(N^+) = T_e(O^+) = f[T_e(O^{+2})]$ , from Pagel et al. (1992), Izotov et al. (1994), and Stasińska & Leitherer (1996). Note that the latter three fits are based on temperatures given by equation (6). Henceforth we will refer to them as pag92, izo94, and sta96.

The following can be noticed when analyzing Figure 3. For a given ion ( $N^+$  or  $O^+$ ),  $T_e$  (vertical axis) at a given  $T_e(O^{+2})$  is in general higher for the n100 models than for the n10 models. This is due to the fact that as  $n(H)$  increases,  $U$  decreases, bringing the regions where  $N^+$  and  $O^+$  are emitting closer to the ionizing source, making them hotter. This behavior is illustrated in Figure 4, which has three panels. The top panel shows  $T_e$  as a function of depth from the illuminated face of the cloud for two models with  $T_{eff} = 43$  kK,  $r_o = 2$  pc, and  $O/H = \text{solar}/50$ , only differing in their value of  $n(H)$ . The lower two panels

show the ionization fractions  $N^+/N$  (solid line) and  $O^+/O$  (dashed line) as functions of depth for the two models. The middle panel corresponds to the n10 model, while the bottom panel corresponds to the n100 model. The dotted lines clearly show that  $T_e$  at the peak of  $N^+/N$  is higher by roughly 1000 K for the n100 model. The same is true for  $T_e$  at the peak of  $O^+/O$ .

Also in Figure 3 we see that for a given value of  $n(H)$ ,  $T_e(N^+)$  is in general lower than  $T_e(O^+)$  [except for the two models with  $T_{eff} = 43$  kK,  $r_o = 2$  pc, and  $O/H = \text{solar}/5$ , for which they are almost identical]. This is shown more clearly in Figure 5, which features  $T_e(N^+)$  vs.  $T_e(O^+)$  for all models, and is a result of the fact that the regions where  $N^+$  and  $O^+$  emit do not completely overlap, the  $O^+$  region extending more towards the star into hotter gas, as we pointed out earlier in our discussion of Figure 4. Our models also indicate that this offset becomes larger with rising stellar temperature and falling metallicity.

In order to show that it is better to use  $T_e(N^+)$  independent of  $T_e(O^+)$  when determining the  $N^+/O^+$  ratios of low metallicity systems, we derived the  $N^+/O^+$  ratios of our sample objects using three different methods but always adopting  $N_e = 100 \text{ cm}^{-3}$ . Methods 1 and 2 both assume that  $T_e(N^+) = T_e(O^+)$ , the assumption frequently made by researchers in the past. In method 1, both temperatures are computed using equation (10), while in method 2 equation (11) is used instead. Then values of  $N^+/H^+$ ,  $O^+/H^+$ , and ultimately  $N^+/O^+$  are determined from these derived temperatures. Finally, method 3 uses equations (10) and (11) to compute  $N^+/H^+$ ,  $O^+/H^+$ , respectively. The resulting three sets of  $N^+/O^+$  ratios are shown in Figure 6. The top panel is a plot of method 1 versus method 3, while the bottom panel is a plot of method 2 versus method 3. We see that using either method 1 or 2 results in systematically underestimating the  $N^+/O^+$  ratios by roughly .05-.10 dex. Therefore, in order to minimize uncertainties in determining  $N^+/O^+$  in low metallicity systems, one clearly should derive  $T_e(N^+)$  and  $T_e(O^+)$  from  $T_e(O^{+2})$  separately.

A comparison of our temperature parameterizations (eqs. [8] and [9]) with those of pag92 and izo94 in Figure 3 shows good agreement among the three functions at a density of  $10 \text{ cm}^{-3}$ , where the pag92 and izo94 formulations are based on photoionization models by Stasińska (1990), most of which have  $n(H) = 10 \text{ cm}^{-3}$ . On the other hand, for a density of  $100 \text{ cm}^{-3}$  the agreement between our results (eqs. [10] and [11]) and pag92 and izo94 is less satisfactory. For the temperature formulation by sta96, there is relatively poor agreement with our low density results for  $T_e(N^+)$  and  $T_e(O^+)$ , although the agreement is better for our results for a density of  $100 \text{ cm}^{-3}$ , especially in the case of  $T_e(O^+)$ . Differences between the  $N^+/O^+$  values obtained with sta96 and our method are due to the fact that sta96 constitutes an extrapolation to lower metallicities of the published relation. In addition, the latter is based on simulations of H II regions created by an evolving group of stars, while we use single non-evolving star simulations. Finally, our method uses independent relations

for  $T_e(\text{N}^+)$  and  $T_e(\text{O}^+)$  with respect to  $T_e(\text{O}^{+2})$ . To test the impact of the density effect on our final  $\text{N}^+/\text{O}^+$  values, we used equation (1) to calculate this ratio for each of our sample objects for the two density regimes, n10 and n100. The results are shown in the upper left panel of Figure 7, where the n100 regime (ordinate) is plotted against the n10 regime (abscissa). Clearly, the points closely follow the diagonal line corresponding to equal values of  $\text{N}^+/\text{O}^+$  in both cases.

Further comparisons of our temperature method with the three literature results just discussed are shown in the remaining panels of Figure 7. In each case we have calculated  $\text{N}^+/\text{O}^+$  values at a density of  $10 \text{ cm}^{-3}$  for our sample objects using both our temperature method (vertical axis) and that of pag92 (upper right), izo94 (lower left), and sta96 (lower right), shown on the horizontal axis in each graph. The diagonal lines show the one-to-one relation. Note the particularly poor agreement between our method and those of pag92 and izo94, especially for  $\text{N}^+/\text{O}^+$  values below -1.2. This disagreement can be easily traced to the relatively low  $T_e(\text{O}^+)$  temperatures predicted by pag92 and izo94 when  $T_e(\text{O}^{+2})$  exceeds 14000 K, resulting in higher  $\text{O}^+/\text{H}^+$  and lower  $\text{N}^+/\text{O}^+$  ratios than ours. On the other hand, the apparently closer agreement with sta96 arises because their parameterizations for both  $T_e(\text{N}^+)$  and  $T_e(\text{O}^+)$  are offset from our curves by roughly the same amount in each case, resulting in relatively little difference in our computed  $\text{N}^+/\text{O}^+$  ratios.

Since in general the only  $N_e$  sensitive line flux ratio available from observations is the [S II] ratio  $I_{6716}/I_{6731}$ , we assumed that  $N_e$  was equal to  $N_e([\text{S II}])$  throughout the observed H II regions. For 42 low metallicity systems in our sample the [S II] ratio was detected with reasonable S/N. For this group of objects,  $N_e([\text{S II}])$  was computed by applying Brent’s method as described above, but replacing  $R_{mod}$  with the observed value,  $R_{obs}$ . We proceeded as follows. We first fixed  $N_e$  at  $100 \text{ cm}^{-3}$  (a typical value for H II regions) and used  $R_{obs}[\text{O III}]$  and equation (7) to determine  $T_e(\text{O}^{+2})$ . Next, from  $T_e(\text{O}^{+2})$ ,  $R_{obs}[\text{S II}]$  and equation (7) we computed  $N_e$ . This new value of  $N_e$  was then employed in the derivation of the N and O abundances of the above 42 objects. For the remaining objects, we used the average  $N_e$  found for this subsample, i.e.,  $\sim 200 \text{ cm}^{-3}$ .

Our final values for  $N_e$ ,  $T_e(\text{O}^{+2})$ ,  $T_e(\text{O}^+)$ , and  $T_e(\text{N}^+)$  are listed for each object in our sample in columns (2) through (5) in Table 5.

Finally, we used our models to derive an ICF for obtaining N/O from  $\text{N}^+/\text{O}^+$ . This was accomplished by computing the average of  $(\text{N/O})/(\text{N}^+/\text{O}^+)$  for the n100 models, where relevant line fluxes and parameterizations were employed to obtain each  $\text{N}^+/\text{O}^+$  ratio, while N/O was fixed and given by the input value to our models, i.e.,  $\log(\text{N/O}) = -1.46$ . The average ICF for these models is 1.08 with a standard deviation of 0.09. This contrasts with common practice which is to use  $\text{ICF} = 1$ .

Unfortunately, the ICF depends on the method employed to compute  $N^+/O^+$ . A common practice is to compute  $N^+/O^+$  from the ion fractions  $\langle N^+/N \rangle$  and  $\langle O^+/O \rangle$  given by:

$$\left\langle \frac{A^{+j}}{A_{tot}} \right\rangle \equiv \frac{\int A^{+j} N_e dV}{\int A_{tot} N_e dV}, \quad (12)$$

and the input values of N and O. A comparison between the  $N^+/O^+$  ratios that we used to compute our final ICF, and those given by equation (12), is shown in Figure 8. In this figure, the difference between  $\log(N^+/O^+)$  and  $\log(\langle N^+/O^+ \rangle)$  is plotted against  $\log(\langle N^+/O^+ \rangle)$ . The latter value is that predicted by equation (12), while  $\log(N^+/O^+)$  is the value obtained from relevant line flux ratios and the temperature parameterizations for the n100 models. Note that Figure 8 illustrates the need of an ICF for obtaining N/O at low metallicities, no matter which method is used to compute it. Clearly,  $\log(\langle N^+/O^+ \rangle)$  deviates from  $\log(N/O)$  which as mentioned above is fixed at -1.46 for all models. In fact, the use of  $\langle N^+/O^+ \rangle$  when computing the ICF results in an average of 1.28 with a standard deviation of 0.1.

The vertical difference in Figure 8 is at most  $\sim 0.11$  dex. It is positive because  $N^+/O^+$  values from line flux ratios and parameterized temperatures are higher than those predicted by equation (12). This fact is reflected in the smaller ICF obtained when using line flux ratio  $N^+/O^+$  values. Since our method is consistent with the way in which  $N^+/O^+$  is measured observationally, i.e., from line flux ratios, we applied an ICF of 1.08 when deriving the N/O abundances of our sample objects. The ICF's contribution to the final N/O uncertainties was accordingly taken to be  $\pm 0.09$ .

### 3. IONIC AND ELEMENTAL ABUNDANCES

We used the above results for density, temperatures, and ICF determinations to derive new values for the O/H and N/O ratios for our sample objects. The corresponding uncertainties were obtained using standard error propagation, where the quantities considered in our estimation of the abundance errors is given in Table 4. The quantities listed in column (1) were assumed to be functions of the variables given in column (2). Note that because  $N_e$  depends on  $T_e$  and visa versa, and since in addition,  $N_e$  had to be assumed for a significant number of objects (see below),  $N_e$  does not appear in Table 4.

For each object in our sample, Table 5 gives the object name in column (1),  $N_e$  in column (2),  $T_e(O^{+2})$ ,  $T_e(O^+)$ , and  $T_e(N^+)$  in columns (3), (4), and (5), respectively, and  $O^+/H^+$ ,  $O^{+2}/H^+$ , and  $N^+/H^+$  in columns (6), (7), and (8), respectively. Our final abundance results are given in Table 6, which lists object name in column (1), references for the observed emission-line strengths in column (2), our derived values for  $12 + \log(O/H) \pm \sigma$  and  $\log(N/O)$

$\pm \sigma$  in columns (3) and (4), and literature values and references in columns (5), (6), and (7), respectively.

Figures 9 and 10 feature comparisons of our O/H and N/O values (vertical axes) against published values. The diagonals show points of one-to-one correspondence. Our O/H values are systematically lower with respect to past calculations due primarily to our new temperature scheme for calculating  $O^+/H^+$ . However, in general, the error bars show agreement between our results and literature values. Our N/O values are also offset (higher by  $\sim 0.05$  to 0.1 dex) due the use of new temperature parametrizations and an ICF for obtaining N/O.

In Figure 11, we plot our uncertainties in  $\log(N/O)$  against corresponding literature values. Some of the published uncertainties were estimated using Monte Carlo simulations to propagate the errors in the relevant line strengths (Campbell et al. 1986; Kobulnicky & Skillman 1996), and thus points occupy both sides of the diagonal due to the random nature of the latter technique. We point out that  $\log(N/O)$  values with small uncertainties generally correspond to objects with small uncertainties in relevant emission-line strengths. The tendency for our error estimates to systematically exceed published ones is primarily due to the contribution of ICF uncertainty for each of our objects. However, we strongly argue that inclusion of this additional factor produces more realistic uncertainties than those previously published.

#### 4. ANALYSIS

Figure 12 is a plot of N/O versus O/H for the abundances and uncertainties listed in Table 6. Recall that N/O is a ratio which measures differential nucleosynthesis, while O/H is a metallicity gauge and measures the extent of chemical evolution in the area immediately surrounding the observed emission-line region. Furthermore, each data point in Figure 12 provides a snapshot of current conditions within a galaxy, each of which arrived at its present position by following a path determined by its own unique star formation history.

Figure 13 shows the distribution of N/O values for our sample, using a bin size of 0.02 dex. Two distinct groups of objects are apparent. The larger population comprises objects extending over the entire O/H range considered here and possessing N/O values which appear to be distributed in near-Gaussian fashion between limits of  $-1.54 \leq N/O \leq -1.27$ . These limits are indicated with dashed lines in Figures 12 and 13. The remaining objects with  $N/O > -1.27$  appear to belong to a smaller population which is concentrated at the high end of our O/H range and possess relatively high N/O values compared with the larger group.

The 52 objects making up the larger population form what we will define for purposes of analysis as the *N/O plateau*. The N/O plateau has been discussed by numerous authors, including Garnett (1990); Thuan et al. (1995), Kobulnicky & Skillman (1996), and Pilyugin et al. (2003). We argue that by treating this group of objects separately, we are not doing so in an arbitrarily fashion. Rather we are led to this result for the following reasons. First, the distribution of the entire sample in the N/O dimension shown in Figure 13 strongly hints at the existence of two distinct groups of objects. Second, our current theoretical understanding of N production strongly suggests that we should expect a narrow, horizontal track at low metallicities where the production is primary. Both analytical and numerical models such as those presented in Henry et al. (2000) predict the presence of this track. Finally, a theoretical analysis of the N/O plateau shape by Henry, Nava, & Prochaska (2006) using numerical chemical evolution models finds that an additional N production process triggered at  $O/H > 7.8$  is needed to explain the high N/O objects. Thus, we conclude that current observational and theoretical evidence suggests that what we have defined as the N/O plateau consists of objects which have been subjected to similar N production mechanisms, and that we are justified in excluding, for the time being, those objects in the smaller group which possess higher N/O ratios.

We now discuss some of the statistical aspects of our measurements. In doing so we note that all means, errors, and standard deviations relating to our sample and given below were initially computed in linear space and then converted to their corresponding logarithmic quantities. This is not necessarily true for values quoted from other papers, however.

The log of the weighted mean of N/O for the 52 objects lying on the plateau is  $-1.43 (+.0084/-0.0085)$ , where the values in parenthesis represent the error in the mean, not the standard deviation, and were derived from observational uncertainties quoted in column (4) of Table 6<sup>6</sup>. The value for plateau objects with O/H below 7.8 is  $-1.44 (+.011/-0.012)$ , while above 7.8 it is measured to be  $-1.41 (+.012/-0.013)$ , so there is no evidence of metallicity dependence of the mean. These results are in good agreement with those of Izotov et al. (1999), who obtained  $-1.47 (\sigma = \pm 0.14)$  for their total sample,  $-1.60 (\sigma = \pm 0.02)$  for their low metallicity ( $O/H < 7.6$ ) objects, and  $-1.46 (\pm 0.14)$  for their high metallicity ( $O/H > 7.6$ ) objects. Likewise, our results are in close agreement with Garnett (1990), who found  $\log(N/O) = -1.46 (+.10/-0.13)$  for plateau objects. Finally, the standard deviation about the weighted mean for our plateau objects, expressed logarithmically, is  $+0.071/-0.084$ , nearly an order of magnitude larger than the error in the mean.

---

<sup>6</sup>Note that the error in the mean depends upon the uncertainties in the individual measurements as well as the square root of the number of objects in the sample, being inversely related to the latter (see Bevington & Robinson 2003).

An interesting question pertaining to the distribution of points in the N/O-O/H plane concerns the nature of the observed N/O scatter (as measured by the standard deviation) of the plateau objects and to what degree it is related to errors in abundance measurements. That is to say, is the spread in N/O associated with the plateau due mostly to intrinsic or statistical scatter? To investigate this point further, we assumed a Gaussian distribution in the parent N/O plateau population, as suggested by the distribution shape in Figure 13, and performed a  $\chi$ -square analysis of the observed point distribution of  $\log(\text{N/O})$  for the plateau using our calculated weighted mean value for  $\log(\text{N/O})$  of -1.43 along with the established errors in the abundances, as given in column (4) of Table 6. We found that the value for the reduced  $\chi$ -square<sup>7</sup> for the 52 plateau objects is 1.244, consistent with a probability of about 90% that our sample of objects could not have been drawn randomly from a parent population characterized by our calculated mean  $\log(\text{N/O})$ , error, and standard deviation. In other words, some additional scatter is needed to explain the observed spread in N/O<sup>8</sup>.

In order to estimate the magnitude of this additional scatter, we recalculated reduced  $\chi$ -square values for the 52 plateau objects numerous times, each time adding intrinsic scatter to the measurement errors in quadrature to simulate real scatter among the objects, with a target value for the reduced  $\chi$ -square of unity. Such a value was reached when  $\sigma$  for the intrinsic component was 0.024, or about 1/3 of the magnitude of the standard deviation and the typical statistical uncertainties in column (4) of Table 6. Therefore, the implication of this  $\chi$ -square analysis is that only a small portion of the scatter observed for the plateau objects is intrinsic. Considering that the many of the uncertainties associated with the line strengths taken from the literature for our analysis are only estimated and not determined in a rigorous fashion, we cannot conclude with any confidence that a significant portion of the vertical scatter in N/O is real. Rather, the issue can only be decided by using better measurements including well-determined uncertainties in the abundances.

---

<sup>7</sup>The reduced  $\chi$ -square,  $\chi^2_\nu = \frac{1}{N-1} \sum_i \left\{ \frac{1}{\sigma_i^2} [y_i - \mu]^2 \right\}$ , where  $y_i$  and  $\sigma_i$  are the N/O value and uncertainty of the  $i$ th object,  $\mu$  is the sample average, and  $N$  is the number of sample objects. Within the summation, the denominator represents the measurement errors.

<sup>8</sup>Concerned that a few points with small observational uncertainties could be artificially inflating the total  $\chi$ -square value, we calculated each object's contribution to the total  $\chi$ -square and found no points to be excessively high.



## 5. CONCLUSIONS

This paper has been devoted to a detailed review of the method for deriving N and O abundances in low mass emission-line galaxies with  $12 + \log(\text{O}/\text{H}) \leq 8.1$ . These low metallicity systems are classified in the literature as dwarf irregular galaxies, blue compact galaxies, or H II galaxies. The principal motivation for our work was to estimate the contribution of the N/O uncertainties to the scatter among N/O plateau objects in the  $\log(\text{N}/\text{O})$  versus  $12 + \log(\text{O}/\text{H})$  diagram. To carry out this study, we selected a sample of 68 objects from the literature and used their published de-reddened emission-line strengths to calculate a homogeneous set of abundances, paying special attention to the determination of [N II] and [O II] electron temperatures for which the necessary but weak auroral lines are usually absent from the data. In such cases these temperatures, which are needed to compute the abundances of their associated ions ( $\text{N}^+$  and  $\text{O}^+$ ), must be inferred from parametric relations in terms of the more accessible [O III] temperature. We established theoretical relations for the relevant temperatures based on single-star H II region simulations (modeled with CLOUDY) and employing our own input stellar spectra (modeled with PHOENIX). These relations were derived from line flux ratio temperatures in contrast with common practice, which is to use ion and  $N_e$ -weighted volume temperature means. We also used our models to infer an ICF for obtaining N/O from  $\text{N}^+/\text{O}^+$ , and to carefully estimate N/O uncertainties by applying standard error propagation methods. This ICF was derived from line flux ratio ionic abundances, also in contrast with common practice, which is to use  $N_e$ -weighted volume ion fraction means. Our method has the advantage of being consistent with the procedure employed to derive  $T_e(\text{O}^{+2})$  and  $\text{N}^+/\text{O}^+$  from observations, i.e., from line flux ratios. Note that  $\text{N}^+/\text{O}^+$  values from line flux ratios and parameterized temperatures are higher than those predicted by equation (12). However, this fact is taken care of by our value for the ICF.

We conclude the following from our studies:

1.  $T_e(\text{N}^+)$  and  $T_e(\text{O}^+)$  diverge significantly from each other in low metallicity regimes. Therefore, the assumption of previous authors that these two temperatures are equivalent appears to be invalid at low metallicities.
2. A realistic value for the  $\text{N}^+/\text{O}^+$  ionization correction factor is  $1.08 \pm 0.09$ .
3. Our final N/O values are systematically larger than previous results, while we find that O/H is generally below other measurements. This outcome is due to our new temperatures and ICF determinations.
4. The majority (52) of objects in our survey form a relatively flat, horizontal system

in the N/O-O/H plane, consistent with the idea that both N and O production are primary at low metallicity. These galaxies comprise what we define as the N/O plateau.

5. Plateau objects appear to form a Gaussian distribution in  $\log(\text{N/O})$  between -1.54 and -1.27 with the logarithm of the weighted arithmetic average,  $\log(\text{N/O})$ , being -1.43 (+.0084/-.0085) and a standard deviation of +.071/-.084.
6. A  $\chi^2$  analysis of the plateau objects indicates that only a small fraction of the observed scatter in N/O is intrinsic, although this conclusion remains tentative until line strength uncertainties, which are the largest contributors to the abundance uncertainties, can be rigorously determined for a large sample of objects.
7. The remaining 16 sample objects have  $\log(\text{N/O})$  values exceeding -1.27 and therefore reside above the N/O plateau as we define it here.

Abundances of N and O are expected to improve in accuracy and precision as better temperature determinations become possible through the use of large telescopes capable of obtaining high S/N spectral observations of the auroral lines of  $\text{N}^+$  and  $\text{O}^+$ . Until that time, photoionization models of increased sophistication can go a long way toward reducing the uncertainty, as we have shown here.

We are grateful to E. Baron, J. X. Prochaska, Schaerer D., T. Hoffmann, and G. J. Ferland for helpful discussions and comments. This research is supported by NSF grant AST 03-07118 and NASA grant NAG5-3505 to the University of Oklahoma.

## REFERENCES

- Allende Prieto, C., Lambert, D. L., & Asplund, M. 2001, *ApJ*, 556, L63
- . 2002, *ApJ*, 573, L137
- Anders, E., & Grevesse, N. 1989, *Geochim. Cosmochim. Acta*, 53, 197
- Asplund, M. 2004, *A&A*, 417, 769
- Aufdenberg, J. P., Hauschildt, P. H., Baron, E., Nordgren, T. E., Burnley, A. W., Howarth, I. D., Gordon, K. D., & Stansberry, J. A. 2002, *ApJ*, 570, 344

- Bevington, P. R., & Robinson, D. K. 2003, Data reduction and error analysis for the physical sciences (Data reduction and error analysis for the physical sciences, 3rd ed., by Philip R. Bevington, and Keith D. Robinson. Boston, MA: McGraw-Hill, ISBN 0-07-247227-8, 2003.)
- Campbell, A., Terlevich, R., & Melnick, J. 1986, MNRAS, 223, 811
- Chiappini, C., Romano, D., & Matteucci, F. 2003, MNRAS, 339, 63
- Ferland, G. J., Korista, K. T., Verner, D. A., Ferguson, J. W., Kingdon, J. B., & Verner, E. M. 1998, PASP, 110, 761
- Flower, D. R. 1983, Science, 222, 1010
- Garnett, D. R. 1989, ApJ, 345, 282
- . 1990, ApJ, 363, 142
- Grevesse, N., & Sauval, A. J. 1998, Space Science Reviews, 85, 161
- Hauschildt, P. H., & Baron, E. 1999, J. Comp. Applied Math., 109, 41
- . 2004, Mitteilungen der Mathematischen Gesellschaft in Hamburg, Band 23
- Henry, R. B. C., Edmunds, M. G., & Köppen 2000, ApJ, 541, 660
- Holweger, H. 2001, in AIP Conf. Proc. 598: Joint SOHO/ACE workshop "Solar and Galactic Composition", 23–+
- Izotov, Y. I., Chaffee, F. H., Foltz, C. B., Green, R. F., Guseva, N. G., & Thuan, T. X. 1999, ApJ, 527, 757
- Izotov, Y. I., Schaerer, D., & Charbonnel, C. 2001, ApJ, 549, 878
- Izotov, Y. I., Stasińska, G., Guseva, N. G., & Thuan, T. X. 2004, A&A, 415, 87
- Izotov, Y. I., & Thuan, T. X. 1998a, ApJ, 497, 227
- . 1998b, ApJ, 500, 188
- Izotov, Y. I., Thuan, T. X., & Lipovetsky, V. A. 1994, ApJ, 435, 647
- . 1997, Dwarf Galaxies: Probes for Galaxy Formation and Evolution, Joint Discussion 2, 21 August 1997, Kyoto, Japan, meeting abstract., 2

- Kobulnicky, H. A., & Skillman, E. D. 1996, *ApJ*, 471, 211
- . 1998, *ApJ*, 497, 601
- Kunth, D., & Östlin, G. 2000, *A&A Rev.*, 10, 1
- Lamers, H. J. G. L. M., & Cassinelli, J. P. 1999, *Introduction to Stellar Winds*, 1999th edn. (Cambridge: Cambridge University Press)
- Leitherer, C., Schaerer, D., Goldader, J. D., Delgado, R. M. G., Robert, C., Kune, D. F., de Mello, D. F., Devost, D., & Heckman, T. M. 1999, *ApJS*, 123, 3
- Lennon, D. J., & Burke, V. M. 1994, *A&AS*, 103, 273
- McLaughlin, B. M., & Bell, K. L. 1994, *ApJS*, 94, 825
- Melbourne, J., Phillips, A., Salzer, J. J., Gronwall, C., & Sarajedini, V. L. 2004, *AJ*, 127, 686
- Osterbrock, D. E. & Ferland, G. J. 2006, *Astrophysics of gaseous nebulae and active galactic nuclei* (*Astrophysics of gaseous nebulae and active galactic nuclei*, 2nd. ed. by D.E. Osterbrock and G.J. Ferland. Sausalito, CA: University Science Books, 2006.)
- Pagel, B. E. J. 1985, in *Production and Distribution of C, N, O Elements*, 155–170
- Pagel, B. E. J., Simonson, E. A., Terlevich, R. J., & Edmunds, M. G. 1992, *MNRAS*, 255, 325
- Pauldrach, A. W. A., Hoffmann, T. L., & Lennon, M. 2001, *A&A*, 375, 161
- Pilyugin, L. S., Contini, T., & Vílchez, J. M. 2004, *A&A*, 423, 427
- Pilyugin, L. S., Thuan, T. X., & Vílchez, J. M. 2003, *A&A*, 397, 487
- Press, W. H., Teukolsky, S. A., Vetterling, W. T., & Flannery, B. P. 1996, *Numerical Recipes in Fortran 90: The Art of Parallel Scientific Computing*, 2nd edn. (Cambridge CB2 1RP: Cambridge University Press)
- Ramsbottom, C. A., Bell, K. L., & Stafford, R. P. 1996, *Atomic Data and Nuclear Data Tables*, 63, 57
- Rubin, R. H. 1986, *ApJ*, 309, 334
- Savage, B. D., & Sembach, K. R. 1996, *ARA&A*, 34, 279

- Schaerer, D., & de Koter, A. 1997, *A&A*, 322, 598
- Shields, G. A., Aller, L. H., Keyes, C. D., & Czyzak, S. J. 1981, *ApJ*, 248, 569
- Skillman, E. D., & Kennicutt, R. C. 1993, *ApJ*, 411, 655
- Smith, L. J., Norris, R. P. F., & Crowther, P. A. 2002, *MNRAS*, 337, 1309
- Stasińska, G. 1990, *A&AS*, 83, 501
- Stasińska, G., & Izotov, Y. 2003, *A&A*, 397, 71
- Stasińska, G., & Leitherer, C. 1996, *ApJS*, 107, 661
- Storey, P. J. & Hummer, D. G. 1995, *MNRAS*, 272, 41
- Thuan, T. X., Izotov, Y. I., & Lipovetsky, V. A. 1995, *ApJ*, 445, 108
- Walsh, J. R., & Roy, J.-R. 1989, *MNRAS*, 239, 297

Table 1. ATOMIC DATA

Ion	Energy Levels	Transition Rates	Collision Strengths (at $10^4$ K)
N <sup>+</sup>	Nist	Nist	Lennon & Burke 1994
O <sup>+</sup>	Nist	Nist	McLaughlin & Bell 1994
O <sup>+2</sup>	Nist	Nist	Lennon & Burke 1994
S <sup>+</sup>		Flower 1983	Ramsbottom et al. 1996

Table 2. PHOENIX MODELS

Star	Metal abundances <sup>a</sup>	$\log(\dot{M})$ ( $M_{\odot} \text{ yr}^{-1}$ )	$v_{\infty}$ ( $\text{km s}^{-1}$ )	$T_{eff}$ ( $10^4 \text{ K}$ )	$\log(g)$ ( $\text{cm s}^{-1}$ )	$R/R_{\odot}$ ( $R_{\odot}=6.95 \times 10^{10} \text{ cm}$ )	$\log(L)$ ( $\text{erg s}^{-1}$ )
1	solar/5	-6.80	2330	4.265	4.00	10.48	38.954 (-3.517/0.960)
2	solar/20	-7.28	1940	4.260	4.00	10.48	39.080 (-3.517/0.960)
3	solar/50	-7.40	1727	4.260	4.00	10.48	39.042 (-3.517/0.960)
4	solar/5	-6.41	2550	5.000	4.00	9.80	39.560 (-2.040/0.960)
5	solar/20	-6.89	2130	5.000	4.00	9.80	39.500 (-3.040/0.960)
6	solar/50	-7.21	1894	5.000	4.00	9.80	39.300 (-2.040/0.960)

<sup>a</sup>Except those of N and C which in order to match typical values measured in low metallicity systems, were set such that  $\log(\text{N/O})=-1.46$  and  $\log(\text{C/O})=-0.7$ .

Table 3. CLOUDY MODELS

Star <sup>a</sup>	$12 + \log(\text{O}/\text{H})$	$n(\text{H})$ ( $\text{cm}^{-3}$ )	$r_0$ (pc)	$\log(\text{U})$	Geometry
1	8.0	10	2	-1.37	spherical
1	8.0	10	5	-2.17	thick shell
1	8.0	100	2	-2.37	thick shell
1	8.0	100	5	-3.17	plane-parallel
2	7.4	10	2	-1.14	spherical
2	7.4	10	5	-1.94	thick shell
2	7.4	100	2	-2.14	thick shell
2	7.4	100	5	-2.94	thick shell
3	7.0	10	2	-1.16	spherical
3	7.0	10	5	-1.96	thick shell
3	7.0	100	2	-2.16	thick shell
3	7.0	100	5	-2.96	plane-parallel
4	8.0	10	2	-0.39	spherical
4	8.0	10	5	-1.19	spherical
4	8.0	100	2	-1.39	thick shell
4	8.0	100	5	-2.19	thick shell
5	7.4	10	2	-0.42	spherical
5	7.4	10	5	-1.22	spherical
5	7.4	100	2	-1.42	thick shell
5	7.4	100	5	-2.22	thick shell
6	7.0	10	2	-0.68	spherical
6	7.0	10	5	-1.48	spherical
6	7.0	100	2	-1.68	thick shell
6	7.0	100	5	-2.48	thick shell

<sup>a</sup>The nebular and stellar abundances are identical for all elements except for Na, Mg, Al, Si, Ca and Fe, whose abundances are  $0.1 \times$  their stellar value.



Table 4. ERROR PROPAGATION

Quantity	Contributing Factors
$R[\text{O III}]$	$I_{4363}, I_{4959}, I_{5007}$
$T_e(\text{O}^{+2})$	$R[\text{O III}]$
$T_e(\text{O}^+)$	$T_e(\text{O}^{+2})$
$T_e(\text{N}^+)$	$T_e(\text{O}^{+2})$
$\text{O}^{+2}/\text{H}^+$	$I_{5007}, T_e(\text{O}^{+2})$
$\text{O}^+/\text{H}^+$	$I_{3727}, T_e(\text{O}^{+2})$
$\text{N}^+/\text{H}^+$	$I_{6584}, T_e(\text{O}^{+2})$
$\text{O}/\text{H}$	$\text{O}^+, \text{O}^{+2}$
$\text{N}/\text{O}$	$\text{ICF}, \text{N}^+/\text{H}^+, \text{O}^+/\text{H}^+$

Table 5. PHYSICAL CONDITIONS AND IONIC ABUNDANCES

Object Names	$N_e$ ( $\text{cm}^{-3}$ )	$T_e(\text{O}^{+2})$ (K)	$T_e(\text{O}^+)$ (K)	$T_e(\text{N}^+)$ (K)	$\text{O}^+/\text{H}^+$ ( $\times 10^5$ )	$\text{O}^{+2}/\text{H}^+$ ( $\times 10^5$ )	$\text{N}^+/\text{H}^+$ ( $\times 10^5$ )
I ZW 18 NW, MRK 116, 0930+554	<50	$19000 \pm 800$	$15800 \pm 100$	$14900 \pm 100$	$0.178 \pm 0.008$	$1.338 \pm 0.080$	$0.006 \pm 0.000$
I ZW 18 SE, MRK 116, 0930+554	200	$16700 \pm 1400$	$15300 \pm 500$	$14700 \pm 300$	$0.365 \pm 0.045$	$1.539 \pm 0.298$	$0.011 \pm 0.001$
SBS 0335-052	250	$20800 \pm 400$	$15900 \pm 100$	$14600 \pm 100$	$0.201 \pm 0.003$	$1.802 \pm 0.021$	$0.007 \pm 0.002$
SBS 0940+544 N	150	$22100 \pm 600$	$15600 \pm 100$	$14100 \pm 300$	$0.364 \pm 0.017$	$1.971 \pm 0.028$	$0.014 \pm 0.002$
SBS 1159+545	100	$19700 \pm 600$	$15900 \pm 100$	$14900 \pm 100$	$0.460 \pm 0.014$	$2.138 \pm 0.076$	$0.017 \pm 0.002$
SBS 1415+437	50	$18600 \pm 300$	$15800 \pm 100$	$14900 \pm 100$	$0.725 \pm 0.012$	$1.996 \pm 0.047$	$0.025 \pm 0.001$
KISSR 85	750	$18100 \pm 1100$	$15700 \pm 200$	$14900 \pm 100$	$0.819 \pm 0.063$	$2.258 \pm 0.259$	$0.033 \pm 0.005$
UGC 4483, 0832+699	50	$16700 \pm 300$	$15300 \pm 100$	$14700 \pm 100$	$0.803 \pm 0.023$	$2.321 \pm 0.086$	$0.023 \pm 0.001$
TOL 1214-277	200	$19100 \pm 700$	$15800 \pm 100$	$14900 \pm 100$	$0.158 \pm 0.012$	$3.265 \pm 0.178$	$0.007 \pm 0.001$
KISSR 1490	200	$19300 \pm 1100$	$15900 \pm 100$	$14900 \pm 100$	$1.046 \pm 0.049$	$2.465 \pm 0.210$	$0.048 \pm 0.008$
SBS 1211+540	150	$17200 \pm 200$	$15400 \pm 100$	$14800 \pm 100$	$0.485 \pm 0.013$	$3.605 \pm 0.113$	$0.016 \pm 0.001$
KISSR 1013, KISSB 211	400	$18200 \pm 1100$	$15700 \pm 200$	$14900 \pm 100$	$1.573 \pm 0.117$	$2.709 \pm 0.306$	$0.117 \pm 0.010$
SBS 1249+493	200	$16900 \pm 700$	$15300 \pm 200$	$14700 \pm 200$	$0.827 \pm 0.055$	$3.517 \pm 0.333$	$0.026 \pm 0.003$
116+583 B	500	$16800 \pm 900$	$15300 \pm 300$	$14700 \pm 200$	$0.490 \pm 0.040$	$3.922 \pm 0.491$	$0.021 \pm 0.006$
VII Zw 403, 1124+792	<50	$15600 \pm 200$	$14800 \pm 100$	$14300 \pm 100$	$1.128 \pm 0.030$	$3.397 \pm 0.130$	$0.042 \pm 0.002$
TOL 1304-353	200	$18600 \pm 700$	$15800 \pm 100$	$14900 \pm 100$	$0.258 \pm 0.009$	$4.527 \pm 0.373$	$0.011 \pm 0.003$
SBS 1420+544, CG 413	200	$18000 \pm 400$	$15700 \pm 100$	$14900 \pm 100$	$0.402 \pm 0.013$	$4.419 \pm 0.174$	$0.014 \pm 0.002$
SBS 1205+557	200	$16200 \pm 700$	$15100 \pm 300$	$14600 \pm 200$	$1.759 \pm 0.121$	$3.312 \pm 0.345$	$0.067 \pm 0.005$
SBS 1128+573	200	$17000 \pm 600$	$15400 \pm 200$	$14800 \pm 100$	$0.668 \pm 0.035$	$4.587 \pm 0.387$	$0.026 \pm 0.005$
C 1543+091	<50	$16500 \pm 500$	$15200 \pm 200$	$14600 \pm 100$	$0.448 \pm 0.024$	$4.812 \pm 0.403$	$0.026 \pm 0.006$
UM 461, SCHG 1148-020	50	$17200 \pm 400$	$15500 \pm 100$	$14800 \pm 100$	$0.353 \pm 0.016$	$4.934 \pm 0.290$	$0.012 \pm 0.001$

Table 5—Continued

Object Names	$N_e$ ( $\text{cm}^{-3}$ )	$T_e(\text{O}^{+2})$ (K)	$T_e(\text{O}^+)$ (K)	$T_e(\text{N}^+)$ (K)	$\text{O}^+/\text{H}^+$ ( $\times 10^5$ )	$\text{O}^{+2}/\text{H}^+$ ( $\times 10^5$ )	$\text{N}^+/\text{H}^+$ ( $\times 10^5$ )
I ZW 36, MRK 209, HARO 29, 1223+487	50	$16300 \pm 100$	$15100 \pm 100$	$14600 \pm 100$	$0.566 \pm 0.004$	$4.865 \pm 0.048$	$0.023 \pm 0.001$
SBS 1331+493 N	150	$16200 \pm 300$	$15100 \pm 100$	$14600 \pm 100$	$0.723 \pm 0.025$	$4.862 \pm 0.205$	$0.026 \pm 0.002$
MRK 1434, SBS 1030+583	200	$15600 \pm 100$	$14800 \pm 100$	$14300 \pm 100$	$0.849 \pm 0.016$	$4.929 \pm 0.121$	$0.026 \pm 0.001$
MRK 193, SBS 1152+579	150	$16400 \pm 200$	$15200 \pm 100$	$14600 \pm 100$	$0.709 \pm 0.016$	$5.204 \pm 0.145$	$0.032 \pm 0.002$
MRK 71, NGC 2343, 0723+692 B	200	$15000 \pm 300$	$14600 \pm 200$	$14100 \pm 200$	$1.483 \pm 0.071$	$4.637 \pm 0.285$	$0.048 \pm 0.003$
MRK 600, 0248+042	50	$15900 \pm 200$	$14900 \pm 100$	$14500 \pm 100$	$1.069 \pm 0.025$	$5.116 \pm 0.168$	$0.029 \pm 0.001$
MRK 71, NGC 2343, SBS 0749+568 B	200	$15300 \pm 800$	$14600 \pm 400$	$14200 \pm 300$	$1.507 \pm 0.162$	$4.980 \pm 0.711$	$0.065 \pm 0.007$
MRK 36, 1102+294	550	$14900 \pm 400$	$14400 \pm 200$	$14000 \pm 200$	$0.808 \pm 0.058$	$5.722 \pm 0.414$	$0.031 \pm 0.007$
POX 4: C1148-203	<50	$15100 \pm 400$	$14500 \pm 200$	$14100 \pm 200$	$0.755 \pm 0.054$	$5.800 \pm 0.425$	$0.041 \pm 0.002$
MRK 1416, SBC 0917+527	200	$15200 \pm 300$	$14600 \pm 200$	$14200 \pm 100$	$1.734 \pm 0.072$	$4.885 \pm 0.268$	$0.050 \pm 0.002$
MRK 71, NGC 2343, 0723+692 A	100	$15900 \pm 100$	$14900 \pm 100$	$14500 \pm 100$	$0.505 \pm 0.003$	$6.132 \pm 0.054$	$0.020 \pm 0.001$
SBS 1533+574 A	<50	$14500 \pm 600$	$14100 \pm 400$	$13800 \pm 300$	$2.431 \pm 0.226$	$4.573 \pm 0.505$	$0.112 \pm 0.007$
MRK 1486, SBS 1358+576	<50	$14800 \pm 200$	$14300 \pm 200$	$14000 \pm 100$	$1.575 \pm 0.054$	$5.530 \pm 0.235$	$0.096 \pm 0.003$
SBS 1331+493 A	200	$13600 \pm 900$	$13500 \pm 700$	$13300 \pm 600$	$2.837 \pm 0.506$	$4.278 \pm 0.803$	$0.102 \pm 0.013$
KISSR 675, KISSB 187	1000	$15200 \pm 1100$	$14600 \pm 600$	$14200 \pm 500$	$1.356 \pm 0.218$	$5.901 \pm 1.211$	$0.048 \pm 0.013$
FAIRALL 30	100	$14600 \pm 300$	$14200 \pm 200$	$13900 \pm 100$	$1.079 \pm 0.044$	$6.418 \pm 0.373$	$0.059 \pm 0.003$
C 0840+120	200	$14200 \pm 400$	$13900 \pm 300$	$13700 \pm 200$	$1.540 \pm 0.111$	$6.080 \pm 0.482$	$0.064 \pm 0.009$
SBS 0926+606	150	$14400 \pm 200$	$14100 \pm 200$	$13800 \pm 100$	$1.851 \pm 0.072$	$5.812 \pm 0.262$	$0.076 \pm 0.002$
I ZW 49, MRK 59, NGC 4861, ARP 209, 1256+351	100	$14600 \pm 700$	$14200 \pm 500$	$13900 \pm 400$	$2.280 \pm 0.278$	$5.460 \pm 0.767$	$0.108 \pm 0.010$
KISSR 1194	50	$14600 \pm 400$	$14200 \pm 200$	$13900 \pm 200$	$1.976 \pm 0.175$	$5.935 \pm 0.487$	$0.078 \pm 0.008$
KISSR 396, KISSB 145, WAS 81	200	$14100 \pm 500$	$13900 \pm 300$	$13600 \pm 300$	$2.705 \pm 0.232$	$5.352 \pm 0.514$	$0.078 \pm 0.005$

Table 5—Continued

Object Names	$N_e$ ( $\text{cm}^{-3}$ )	$T_e(\text{O}^{+2})$ (K)	$T_e(\text{O}^+)$ (K)	$T_e(\text{N}^+)$ (K)	$\text{O}^+/\text{H}^+$ ( $\times 10^5$ )	$\text{O}^{+2}/\text{H}^+$ ( $\times 10^5$ )	$\text{N}^+/\text{H}^+$ ( $\times 10^5$ )
UM 420, 0218+003	200	$13900 \pm 800$	$13800 \pm 600$	$13500 \pm 500$	$2.754 \pm 0.425$	$5.384 \pm 0.915$	$0.267 \pm 0.026$
1437+370	200	$14200 \pm 300$	$13900 \pm 200$	$13600 \pm 200$	$1.511 \pm 0.079$	$6.699 \pm 0.382$	$0.056 \pm 0.003$
KISSR 1778	50	$13100 \pm 900$	$13100 \pm 700$	$13000 \pm 700$	$3.622 \pm 0.816$	$4.605 \pm 0.968$	$0.149 \pm 0.027$
UM 462, SCHG 1150-021	200	$14300 \pm 200$	$14000 \pm 100$	$13700 \pm 100$	$1.527 \pm 0.050$	$6.841 \pm 0.275$	$0.055 \pm 0.007$
SBS 1222+614	200	$14300 \pm 100$	$14000 \pm 100$	$13700 \pm 100$	$1.231 \pm 0.026$	$7.369 \pm 0.181$	$0.035 \pm 0.001$
TOL 1304-386	100	$14200 \pm 300$	$13900 \pm 200$	$13600 \pm 200$	$1.073 \pm 0.061$	$7.781 \pm 0.502$	$0.082 \pm 0.006$
1533+469	<50	$13900 \pm 500$	$13800 \pm 400$	$13500 \pm 300$	$2.456 \pm 0.257$	$6.514 \pm 0.740$	$0.149 \pm 0.012$
SBS 0907+543	100	$14500 \pm 400$	$14200 \pm 300$	$13900 \pm 200$	$0.939 \pm 0.069$	$8.113 \pm 0.689$	$0.030 \pm 0.005$
UM 469	200	$12900 \pm 1200$	$13000 \pm 1000$	$12800 \pm 900$	$2.458 \pm 0.710$	$6.662 \pm 1.858$	$0.201 \pm 0.039$
1054+365, CG 798	200	$13900 \pm 200$	$13700 \pm 100$	$13500 \pm 100$	$1.210 \pm 0.044$	$8.010 \pm 0.315$	$0.047 \pm 0.002$
MRK 1450, SBS 1135+581	200	$13200 \pm 200$	$13200 \pm 100$	$13000 \pm 100$	$1.764 \pm 0.063$	$7.459 \pm 0.258$	$0.071 \pm 0.002$
MRK 1271, TOL 1053+064	50	$14200 \pm 200$	$13900 \pm 100$	$13600 \pm 100$	$1.677 \pm 0.055$	$7.752 \pm 0.285$	$0.086 \pm 0.003$
NGC 5253-6	100	$12700 \pm 600$	$12800 \pm 500$	$12600 \pm 500$	$4.204 \pm 0.662$	$5.374 \pm 0.793$	$0.284 \pm 0.029$
MRK 1304, UM 448, SCHG 1139+006	100	$12200 \pm 600$	$12400 \pm 500$	$12300 \pm 500$	$4.559 \pm 0.766$	$5.090 \pm 0.756$	$0.496 \pm 0.050$
MRK 22, SBS 0946+558	50	$13500 \pm 200$	$13500 \pm 200$	$13300 \pm 100$	$1.753 \pm 0.078$	$7.896 \pm 0.354$	$0.064 \pm 0.003$
1441+294, CG 1258	200	$13200 \pm 800$	$13200 \pm 600$	$13000 \pm 500$	$1.969 \pm 0.340$	$7.709 \pm 1.326$	$0.087 \pm 0.012$
KISS 49, KISSB 94, CG 177	100	$13100 \pm 800$	$13100 \pm 700$	$13000 \pm 600$	$4.490 \pm 0.888$	$5.229 \pm 1.010$	$0.239 \pm 0.037$
MRK 1409, SBS 0741+535	550	$13700 \pm 700$	$13600 \pm 500$	$13400 \pm 400$	$3.673 \pm 0.486$	$6.132 \pm 0.869$	$0.121 \pm 0.011$
0948+532	100	$13500 \pm 300$	$13400 \pm 200$	$13200 \pm 200$	$1.631 \pm 0.096$	$8.250 \pm 0.492$	$0.069 \pm 0.004$
TOL 1345-420	100	$13400 \pm 700$	$13400 \pm 500$	$13200 \pm 400$	$2.034 \pm 0.279$	$7.939 \pm 1.149$	$0.055 \pm 0.008$
UM 439	600	$14200 \pm 300$	$14000 \pm 200$	$13700 \pm 200$	$0.890 \pm 0.047$	$9.533 \pm 0.579$	$0.034 \pm 0.006$

Table 5—Continued

Object Names	$N_e$ ( $\text{cm}^{-3}$ )	$T_e(\text{O}^{+2})$ (K)	$T_e(\text{O}^+)$ (K)	$T_e(\text{N}^+)$ (K)	$\text{O}^+/\text{H}^+$ ( $\times 10^5$ )	$\text{O}^{+2}/\text{H}^+$ ( $\times 10^5$ )	$\text{N}^+/\text{H}^+$ ( $\times 10^5$ )
TOL 0645-376	350	$12900 \pm 1600$	$13000 \pm 1300$	$12800 \pm 1200$	$3.272 \pm 1.222$	$7.342 \pm 2.632$	$0.254 \pm 0.065$
KISSR 1845, CG 903, HS 1440+4302	50	$13300 \pm 300$	$13300 \pm 200$	$13100 \pm 200$	$2.997 \pm 0.286$	$8.061 \pm 0.622$	$0.111 \pm 0.011$
MRK 5, 0635+756	200	$12200 \pm 500$	$12400 \pm 500$	$12200 \pm 400$	$3.566 \pm 0.515$	$7.512 \pm 0.951$	$0.168 \pm 0.016$
II ZW 40	200	$13300 \pm 200$	$13300 \pm 100$	$13100 \pm 100$	$0.581 \pm 0.026$	$10.780 \pm 0.523$	$0.057 \pm 0.003$
MRK 1089, 0459-043	100	$11100 \pm 700$	$11300 \pm 700$	$11200 \pm 700$	$5.533 \pm 1.432$	$6.302 \pm 1.249$	$0.519 \pm 0.079$

Table 6. ELEMENTAL ABUNDANCES

Object Names	Ref. for $I(\lambda)$	$12 + \log(\frac{O}{H})$ (present work)	$\log(\frac{N}{O})$ (present work)	$12 + \log(\frac{O}{H})$ (literature)	$\log(\frac{N}{O})$ (literature)	Ref. for cols. 5 & 6
I ZW 18 NW, MRK 116, 0930+554	4	$7.181 \pm 0.023$	$-1.416 \pm 0.049$	$7.170 \pm_{0.040}^{0.040}$	$-1.560 \pm_{0.090}^{0.090}$	7
I ZW 18 SE, MRK 116, 0930+554	4	$7.280 \pm 0.069$	$-1.505 \pm 0.070$	$7.260 \pm_{0.050}^{0.050}$	$-1.600 \pm_{0.060}^{0.060}$	7
SBS 0335-052	10	$7.302 \pm 0.005$	$-1.408 \pm 0.104$	$7.290 \pm_{0.010}^{0.010}$	$-1.580 \pm_{0.030}^{0.030}$	11
SBS 0940+544 N	5	$7.368 \pm 0.006$	$-1.382 \pm 0.071$	$7.315 \pm_{0.016}^{0.016}$	$-1.523 \pm_{0.081}^{0.068}$	7
SBS 1159+545	5	$7.415 \pm 0.013$	$-1.397 \pm 0.055$	$7.442 \pm_{0.019}^{0.018}$	$-1.533 \pm_{0.072}^{0.062}$	7
SBS 1415+437	6	$7.435 \pm 0.008$	$-1.423 \pm 0.039$	$7.504 \pm_{0.014}^{0.014}$	$-1.568 \pm_{0.047}^{0.042}$	7
KISSR 85	12	$7.488 \pm 0.038$	$-1.358 \pm 0.078$	$7.500 \pm_{0.060}^{0.060}$	$-1.380 \pm_{0.110}^{0.110}$	12
UGC 4483, 0832+699	5	$7.495 \pm 0.012$	$-1.509 \pm 0.041$	$7.553 \pm_{0.016}^{0.015}$	$-1.629 \pm_{0.060}^{0.053}$	7
TOL 1214-277	1,3	$7.534 \pm 0.023$	$-1.324 \pm 0.069$	$7.576 \pm_{0.026}^{0.025}$	$-1.449 \pm_{0.098}^{0.080}$	7
KISSR 1490	12	$7.546 \pm 0.027$	$-1.300 \pm 0.087$	$7.560 \pm_{0.070}^{0.070}$	$-1.410 \pm_{0.130}^{0.130}$	12
SBS 1211+540	5	$7.612 \pm 0.012$	$-1.458 \pm 0.044$	$7.671 \pm_{0.011}^{0.010}$	$-1.601 \pm_{0.067}^{0.058}$	7
KISSR 1013, KISSB 211	12	$7.632 \pm 0.033$	$-1.095 \pm 0.061$	$7.660 \pm_{0.050}^{0.050}$	$-1.180 \pm_{0.090}^{0.090}$	12
SBS 1249+493	6	$7.638 \pm 0.034$	$-1.468 \pm 0.071$	$7.703 \pm_{0.025}^{0.024}$	$-1.584 \pm_{0.101}^{0.082}$	7
116+583 B	8	$7.645 \pm 0.048$	$-1.326 \pm 0.124$	$7.680 \pm_{0.050}^{0.050}$	$-1.450 \pm_{0.110}^{0.110}$	11
VII Zw 403, 1124+792	8	$7.656 \pm 0.013$	$-1.394 \pm 0.042$	$7.690 \pm_{0.010}^{0.010}$	$-1.530 \pm_{0.030}^{0.030}$	11
TOL 1304-353	1	$7.680 \pm 0.034$	$-1.316 \pm 0.122$	$7.721 \pm_{0.036}^{0.033}$	$-1.442 \pm_{0.181}^{0.127}$	7
SBS 1420+544, CG 413	6	$7.683 \pm 0.016$	$-1.429 \pm 0.082$	$7.728 \pm_{0.014}^{0.014}$	$-1.542 \pm_{0.096}^{0.078}$	7
SBS 1205+557	8	$7.705 \pm 0.031$	$-1.382 \pm 0.056$	$7.750 \pm_{0.030}^{0.030}$	$-1.500 \pm_{0.080}^{0.080}$	11
SBS 1128+573	8	$7.721 \pm 0.032$	$-1.377 \pm 0.090$	$7.750 \pm_{0.030}^{0.030}$	$-1.510 \pm_{0.070}^{0.070}$	11
C 1543+091	1	$7.721 \pm 0.033$	$-1.208 \pm 0.117$	$7.773 \pm_{0.027}^{0.025}$	$-1.340 \pm_{0.156}^{0.115}$	7
UM 461, SCHG 1148-020	1	$7.723 \pm 0.024$	$-1.417 \pm 0.050$	$7.764 \pm_{0.020}^{0.019}$	$-1.579 \pm_{0.068}^{0.059}$	7

Table 6—Continued

Object Names	Ref. for $I(\lambda)$	$12 + \log(\frac{O}{H})$ (present work)	$\log(\frac{N}{O})$ (present work)	$12 + \log(\frac{O}{H})$ (literature)	$\log(\frac{N}{O})$ (literature)	Ref. for cols. 5 & 6
I ZW 36, MRK 209, HARO 29, 1223+487	8	$7.735 \pm 0.004$	$-1.349 \pm 0.039$	$7.770 \pm_{0.010}^{0.010}$	$-1.490 \pm_{0.010}^{0.010}$	11
SBS 1331+493 N	5	$7.747 \pm 0.016$	$-1.410 \pm 0.048$	$7.801 \pm_{0.011}^{0.011}$	$-1.492 \pm_{0.056}^{0.050}$	7
MRK 1434, SBS 1030+583	8	$7.762 \pm 0.009$	$-1.479 \pm 0.040$	$7.790 \pm_{0.010}^{0.010}$	$-1.600 \pm_{0.020}^{0.020}$	11
MRK 193, SBS 1152+579	5	$7.772 \pm 0.011$	$-1.310 \pm 0.043$	$7.865 \pm_{0.010}^{0.010}$	$-1.274 \pm_{0.052}^{0.047}$	7
MRK 71, NGC 2343, 0723+692 B	8	$7.787 \pm 0.021$	$-1.456 \pm 0.049$	$7.810 \pm_{0.020}^{0.020}$	$-1.570 \pm_{0.040}^{0.040}$	11
MRK 600, 0248+042	10	$7.791 \pm 0.012$	$-1.535 \pm 0.040$	$7.830 \pm_{0.010}^{0.010}$	$-1.670 \pm_{0.030}^{0.030}$	11
MRK 71, NGC 2343, SBS 0749+568 B	8	$7.812 \pm 0.049$	$-1.332 \pm 0.075$	$7.850 \pm_{0.050}^{0.050}$	$-1.440 \pm_{0.110}^{0.110}$	11
MRK 36, 1102+294	1	$7.815 \pm 0.028$	$-1.382 \pm 0.111$	$7.847 \pm_{0.023}^{0.022}$	$-1.459 \pm_{0.144}^{0.108}$	7
POX 4: C1148-203	1	$7.817 \pm 0.028$	$-1.233 \pm 0.052$	$7.855 \pm_{0.025}^{0.023}$	$-1.350 \pm_{0.085}^{0.071}$	7
MRK 1416, SBC 0917+527	8	$7.821 \pm 0.018$	$-1.507 \pm 0.044$	$7.860 \pm_{0.020}^{0.020}$	$-1.620 \pm_{0.040}^{0.040}$	11
MRK 71, NGC 2343, 0723+692 A	8	$7.822 \pm 0.004$	$-1.373 \pm 0.040$	$7.850 \pm_{0.010}^{0.010}$	$-1.520 \pm_{0.010}^{0.010}$	11
SBS 1533+574 A	8	$7.845 \pm 0.034$	$-1.303 \pm 0.061$	$7.880 \pm_{0.030}^{0.030}$	$-1.430 \pm_{0.080}^{0.080}$	11
MRK 1486, SBS 1358+576	8	$7.852 \pm 0.015$	$-1.179 \pm 0.042$	$7.880 \pm_{0.010}^{0.010}$	$-1.310 \pm_{0.030}^{0.030}$	11
SBS 1331+493 A	6	$7.852 \pm 0.058$	$-1.408 \pm 0.101$	$7.893 \pm_{0.053}^{0.047}$	$-1.495 \pm_{0.112}^{0.089}$	7
KISSR 675, KISSB 187	12	$7.861 \pm 0.074$	$-1.418 \pm 0.140$	$7.870 \pm_{0.090}^{0.090}$	$-1.390 \pm_{0.180}^{0.180}$	12
FAIRALL 30	1	$7.875 \pm 0.022$	$-1.228 \pm 0.046$	$7.907 \pm_{0.021}^{0.020}$	$-1.339 \pm_{0.076}^{0.064}$	7
C 0840+120	1	$7.882 \pm 0.028$	$-1.347 \pm 0.077$	$7.915 \pm_{0.027}^{0.025}$	$-1.448 \pm_{0.095}^{0.078}$	7
SBS 0926+606	8	$7.884 \pm 0.015$	$-1.349 \pm 0.042$	$7.910 \pm_{0.010}^{0.010}$	$-1.470 \pm_{0.030}^{0.030}$	11
I ZW 49, MRK 59, NGC 4861, ARP 209, 1256+351	13	$7.889 \pm 0.046$	$-1.290 \pm 0.075$	$7.940 \pm_{0.030}^{0.030}$	$-1.440 \pm_{0.060}^{0.050}$	7
KISSR 1194	12	$7.898 \pm 0.028$	$-1.367 \pm 0.068$	$7.920 \pm_{0.040}^{0.040}$	$-1.460 \pm_{0.080}^{0.080}$	12
KISSR 396, KISSB 145, WAS 81	12	$7.906 \pm 0.030$	$-1.508 \pm 0.058$	$7.920 \pm_{0.040}^{0.040}$	$-1.580 \pm_{0.070}^{0.070}$	12

Table 6—Continued

Object Names	Ref. for $I(\lambda)$	$12 + \log(\frac{O}{H})$ (present work)	$\log(\frac{N}{O})$ (present work)	$12 + \log(\frac{O}{H})$ (literature)	$\log(\frac{N}{O})$ (literature)	Ref. for cols. 5 & 6
UM 420, 0218+003	10	$7.911 \pm 0.054$	$-0.979 \pm 0.087$	$7.930 \pm_{0.050}^{0.050}$	$-1.080 \pm_{0.120}^{0.120}$	11
1437+370	5	$7.914 \pm 0.021$	$-1.400 \pm 0.050$	$7.965 \pm_{0.014}^{0.014}$	$-1.488 \pm_{0.060}^{0.053}$	7
KISSR 1778	12	$7.915 \pm 0.067$	$-1.351 \pm 0.131$	$7.930 \pm_{0.080}^{0.080}$	$-1.440 \pm_{0.160}^{0.160}$	12
UM 462, SCHG 1150-021	1	$7.923 \pm 0.015$	$-1.412 \pm 0.071$	$7.960 \pm_{0.018}^{0.017}$	$-1.506 \pm_{0.098}^{0.080}$	7
SBS 1222+614	8	$7.935 \pm 0.009$	$-1.508 \pm 0.039$	$7.950 \pm_{0.010}^{0.010}$	$-1.610 \pm_{0.020}^{0.020}$	11
TOL 1304-386	1	$7.947 \pm 0.025$	$-1.082 \pm 0.055$	$7.982 \pm_{0.021}^{0.020}$	$-1.181 \pm_{0.084}^{0.070}$	7
1533+469	6	$7.953 \pm 0.038$	$-1.183 \pm 0.068$	$8.042 \pm_{0.029}^{0.027}$	$-1.354 \pm_{0.075}^{0.064}$	7
SBS 0907+543	8	$7.957 \pm 0.033$	$-1.461 \pm 0.083$	$8.010 \pm_{0.030}^{0.030}$	$-1.590 \pm_{0.080}^{0.080}$	11
UM 469	1,3	$7.960 \pm 0.095$	$-1.052 \pm 0.156$	$7.982 \pm_{0.080}^{0.068}$	$-1.113 \pm_{0.177}^{0.125}$	7
1054+365, CG 798	8	$7.965 \pm 0.015$	$-1.380 \pm 0.044$	$7.970 \pm_{0.020}^{0.020}$	$-1.480 \pm_{0.030}^{0.030}$	11
MRK 1450, SBS 1135+581	5	$7.965 \pm 0.013$	$-1.363 \pm 0.041$	$8.007 \pm_{0.013}^{0.013}$	$-1.412 \pm_{0.058}^{0.051}$	7
MRK 1271, TOL 1053+064	10	$7.975 \pm 0.013$	$-1.257 \pm 0.042$	$7.990 \pm_{0.010}^{0.010}$	$-1.380 \pm_{0.030}^{0.030}$	11
NGC 5253-6	2	$7.981 \pm 0.047$	$-1.136 \pm 0.089$	$8.006 \pm_{0.045}^{0.041}$	$-1.212 \pm_{0.096}^{0.078}$	7
MRK 1304, UM 448, SCHG 1139+006	10	$7.984 \pm 0.048$	$-0.929 \pm 0.092$	$7.990 \pm_{0.040}^{0.040}$	$-1.010 \pm_{0.010}^{0.100}$	11
MRK 22, SBS 0946+558	5	$7.984 \pm 0.016$	$-1.400 \pm 0.044$	$8.026 \pm_{0.015}^{0.015}$	$-1.495 \pm_{0.059}^{0.052}$	7
1441+294, CG 1258	8	$7.986 \pm 0.061$	$-1.318 \pm 0.103$	$7.990 \pm_{0.060}^{0.060}$	$-1.410 \pm_{0.130}^{0.130}$	11
KISS 49, KISSB 94, CG 177	12	$7.988 \pm 0.060$	$-1.240 \pm 0.115$	$8.000 \pm_{0.060}^{0.060}$	$-1.300 \pm_{0.110}^{0.110}$	12
MRK 1409, SBS 0741+535	8	$7.991 \pm 0.044$	$-1.448 \pm 0.078$	$8.010 \pm_{0.040}^{0.040}$	$-1.540 \pm_{0.100}^{0.100}$	11
0948+532	5	$7.995 \pm 0.022$	$-1.339 \pm 0.050$	$8.032 \pm_{0.015}^{0.015}$	$-1.442 \pm_{0.061}^{0.053}$	7
TOL 1345-420	1	$7.999 \pm 0.051$	$-1.530 \pm 0.092$	$8.033 \pm_{0.041}^{0.038}$	$-1.618 \pm_{0.116}^{0.091}$	7
UM 439	1	$8.018 \pm 0.024$	$-1.385 \pm 0.085$	$8.045 \pm_{0.020}^{0.020}$	$-1.444 \pm_{0.114}^{0.090}$	7



Table 6—Continued

Object Names	Ref. for $I(\lambda)$	$12 + \log(\frac{O}{H})$ (present work)	$\log(\frac{N}{O})$ (present work)	$12 + \log(\frac{O}{H})$ (literature)	$\log(\frac{N}{O})$ (literature)	Ref. for cols. 5 & 6
TOL 0645-376	1	$8.026 \pm 0.119$	$-1.076 \pm 0.200$	$8.046 \pm_{0.102}^{0.083}$	$-1.133 \pm_{0.226}^{0.148}$	7
KISSR 1845, CG 903, HS 1440+4302	12	$8.044 \pm 0.027$	$-1.397 \pm 0.071$	$8.050 \pm_{0.040}^{0.040}$	$-1.470 \pm_{0.080}^{0.080}$	12
MRK 5, 0635+756	10	$8.044 \pm 0.042$	$-1.292 \pm 0.083$	$8.040 \pm_{0.040}^{0.040}$	$-1.360 \pm_{0.100}^{0.100}$	11
II ZW 40	1	$8.055 \pm 0.020$	$-0.974 \pm 0.048$	$8.046 \pm_{0.026}^{0.025}$	$-1.042 \pm_{0.121}^{0.095}$	7
MRK 1089, 0459-043	10	$8.073 \pm 0.070$	$-0.993 \pm 0.135$	$8.040 \pm_{0.060}^{0.060}$	$-1.050 \pm_{0.140}^{0.140}$	11

REFERENCES.—(1)Campbell et al. 1986;(2)Walsh & Roy 1989;(3)Pagel et al. 1992;(4)Skillman & Kennicutt 1993;(5)Izotov et al. 1994;(6)Thuan et al. 1995;(7)Kobulnicky & Skillman 1996;(8)Izotov et al. 1997; (9)Izotov & Thuan 1998a; (10)Izotov & Thuan 1998b; (11)Izotov et al. 1999;(12)Melbourne et al. 2004;(13)Kobulnicky & Skillman 1998.

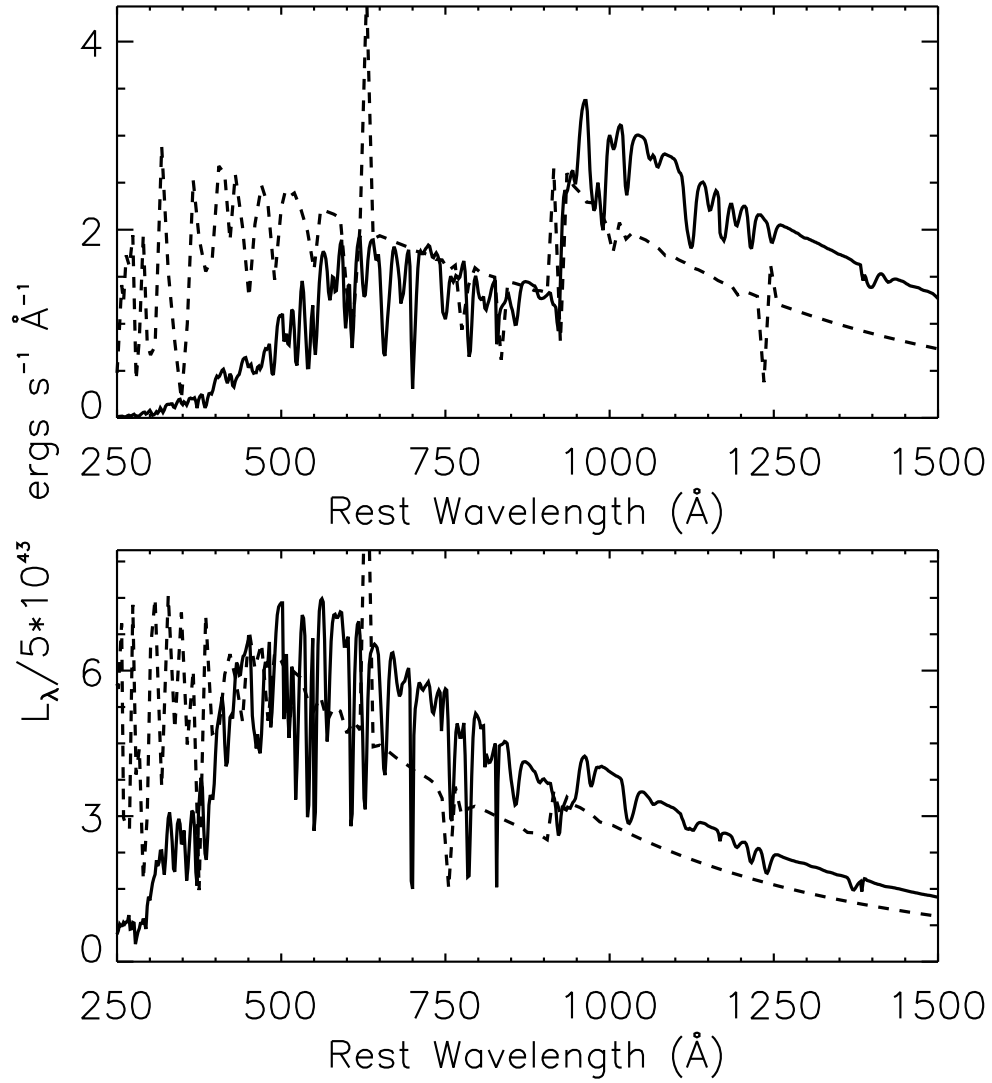


Fig. 1.— Modeled spectra generated with PHOENIX (solid lines) and with *WM-Basic* (dashed lines) for two O-dwarfs having  $O/H = \text{solar}/20$ . The top panel features a 43 kK star, while the bottom panel features a 50 kK star.

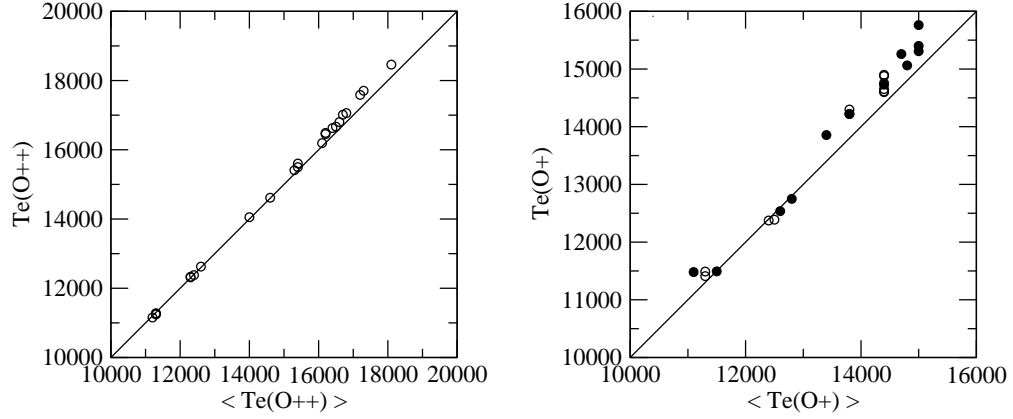


Fig. 2.— Left:  $T_e(O^{+2})$  from  $R[O\ III]$  (vertically) vs.  $T_e(O^{+2})$  from eq. [6] (horizontally) for each model. Right: Parameterized  $T_e(O^+)$  (vertically) vs.  $T_e(O^+)$  from eq. [6] (horizontally). For the parameterized  $T_e(O^+)$ , we used eq. [9] for the n10 models (open circles) and eq. [11] for the n100 models (closed circles).

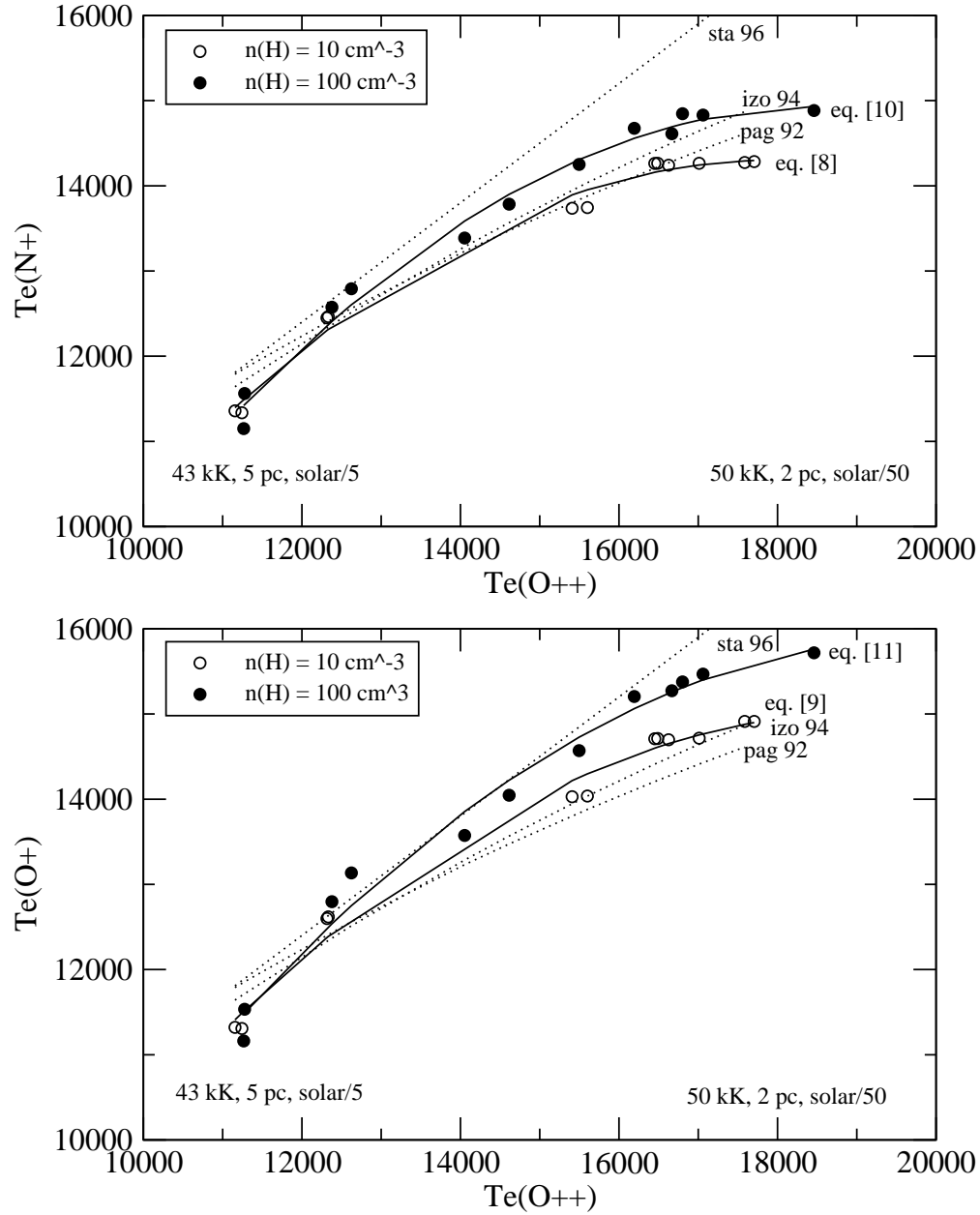


Fig. 3.— Electron temperature parameterizations given by our models (solid lines), and by pag92, izo94, and sta96 (dotted lines). The solid lines labeled eq. [8] (top panel) and eq. [9] (bottom panel) are best fits to n10 models (open circles). The solid lines labeled eq. [10] (top panel) and eq. [11] (bottom panel) are best fits to n100 models (closed circles).  $T_{eff}$ ,  $r_o$ , and O/H are indicated for the models located at the two  $T_e(O^{+2})$  extrema.

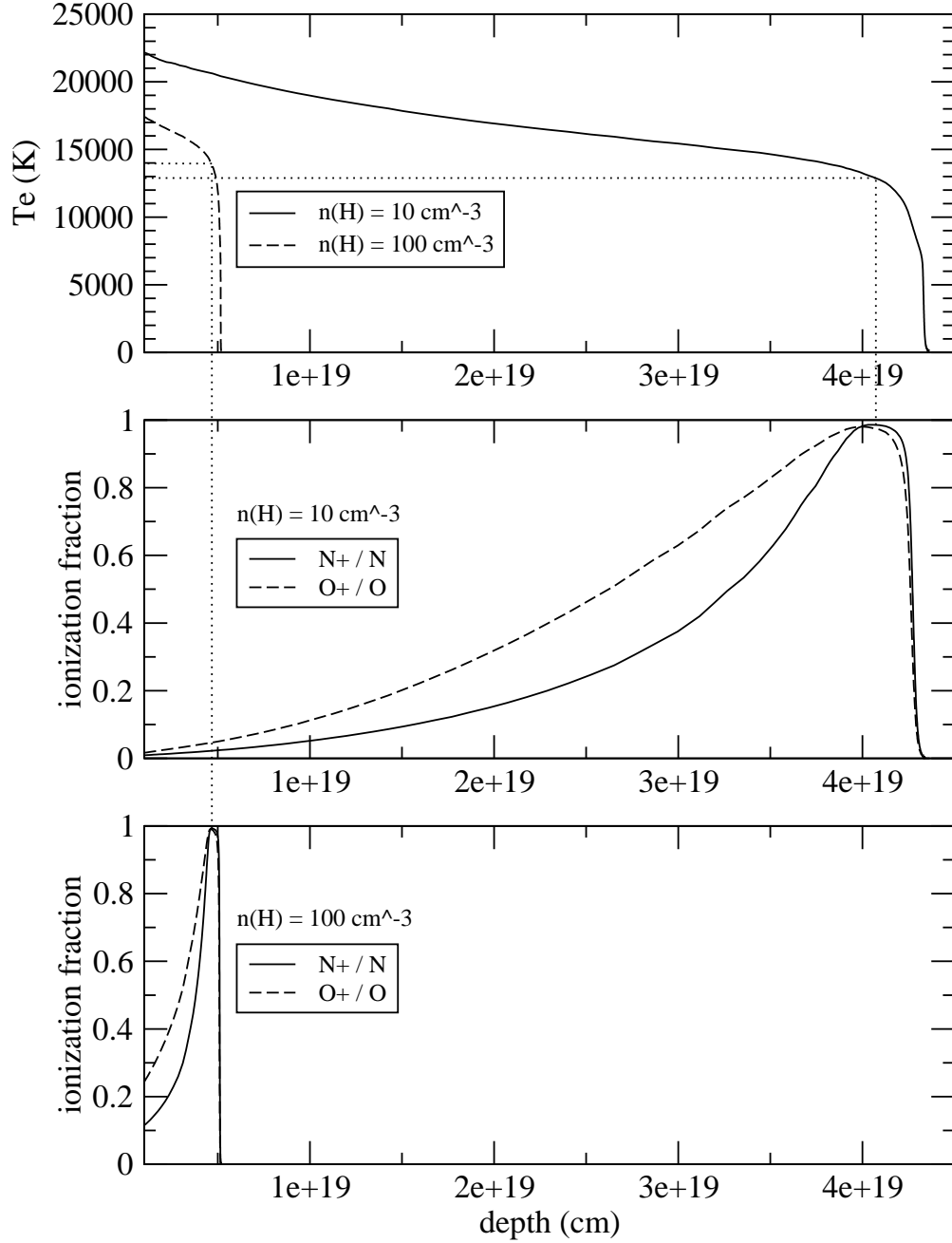


Fig. 4.— Example of how  $T_e$ ,  $N^+/N$ , and  $O^+/O$  vary with depth as  $n(H)$  increases. The two models shown have  $T_{eff} = 43 \text{ kK}$ ,  $r_o = 2 \text{ pc}$ ,  $O/H = \text{solar}/50$ , and they differ only in their value of  $n(H)$ . The solid and dashed lines in the top panel give the  $T_e$ -structure for the n10 and n100 models (respectively), while they correspond to  $N^+/N$  and  $O^+/O$  in the middle (n10 model) and bottom (n100 model) panels. The dotted lines lead to  $T_e$  at  $Max\{N^+/N\}$  for each model.

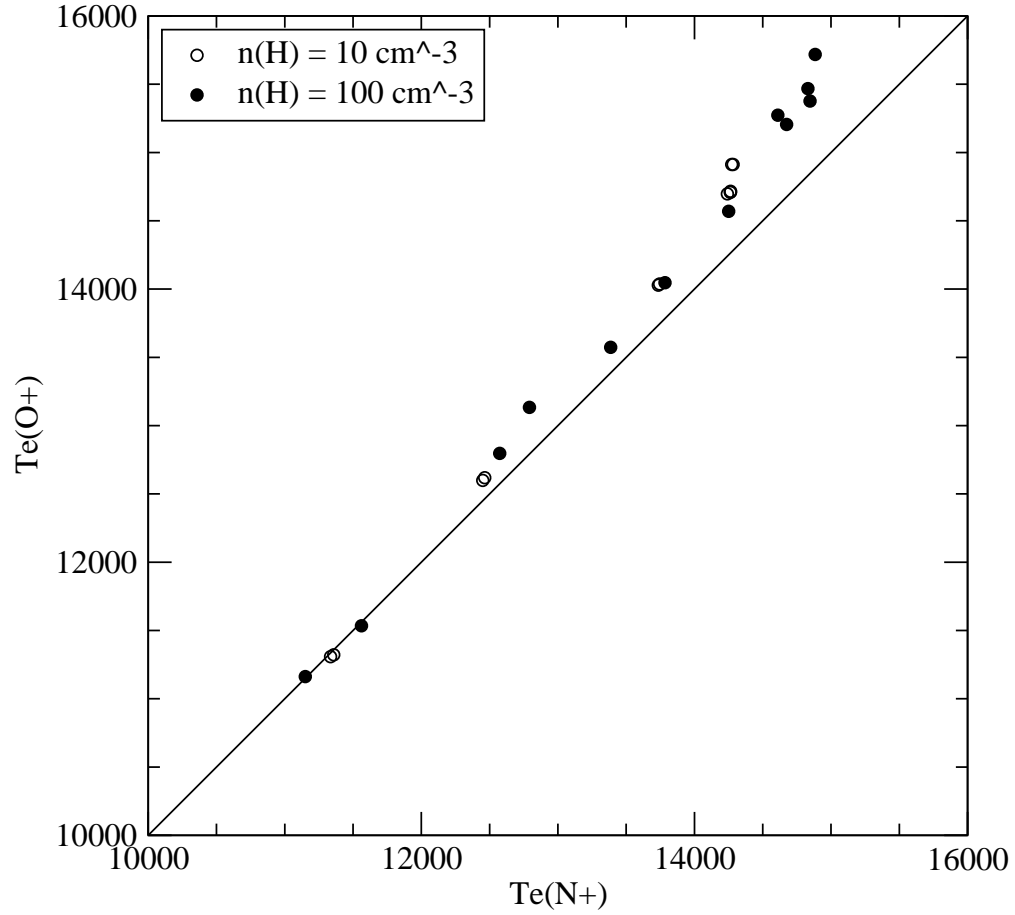


Fig. 5.— Diagram showing  $T_e(O^+)$  vs.  $T_e(N^+)$ , where the temperatures were obtained using line flux ratios from our 24 models. Models with  $n(H) = 10 \text{ cm}^{-3}$  are shown with open circles, while models with  $n(H) = 100 \text{ cm}^{-3}$  are shown with filled circles. The diagonal corresponds to points such that  $T_e(N^+) = T_e(O^+)$ .

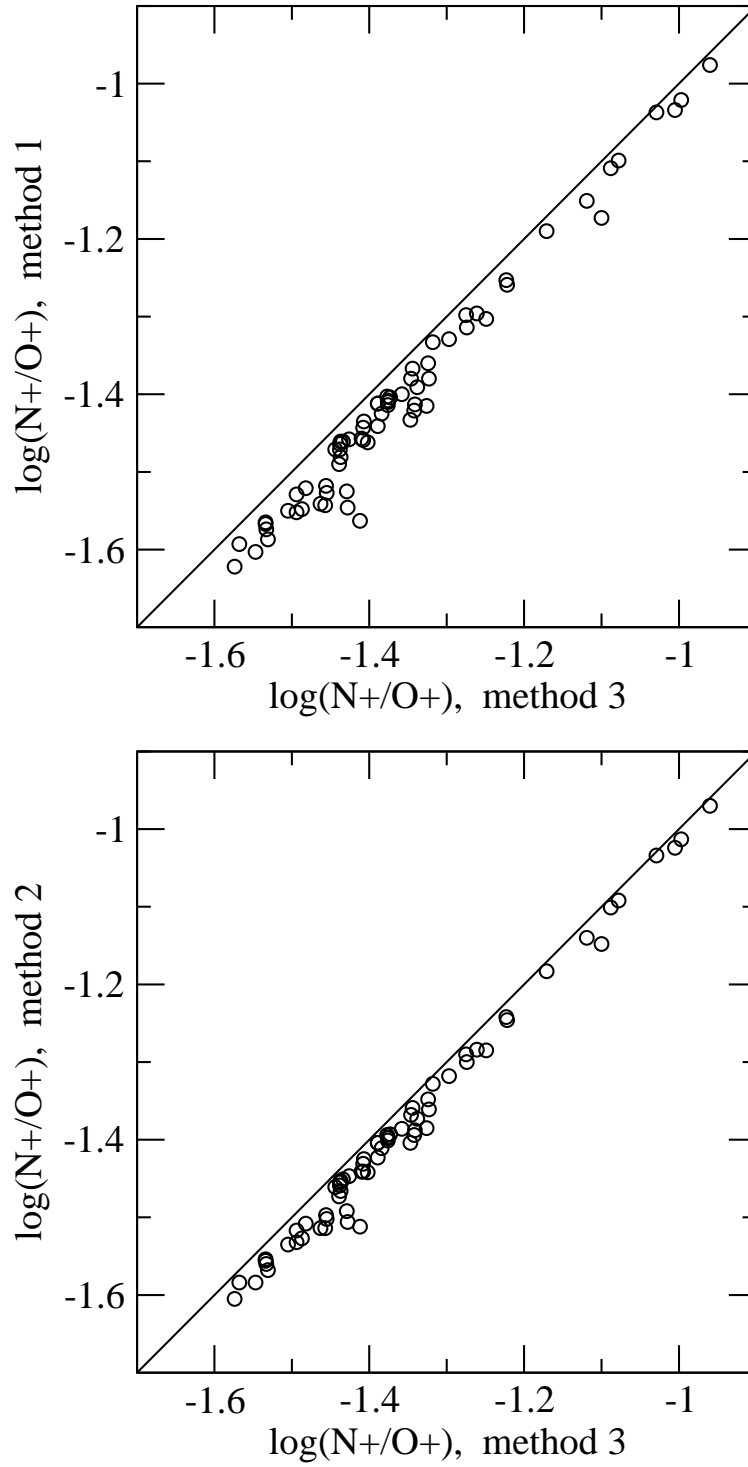


Fig. 6.— Comparison of  $N^+/O^+$  ratios derived for our sample objects. The top panel shows method 1 vs. method 3, while the bottom panel shows method 2 vs. method 3.

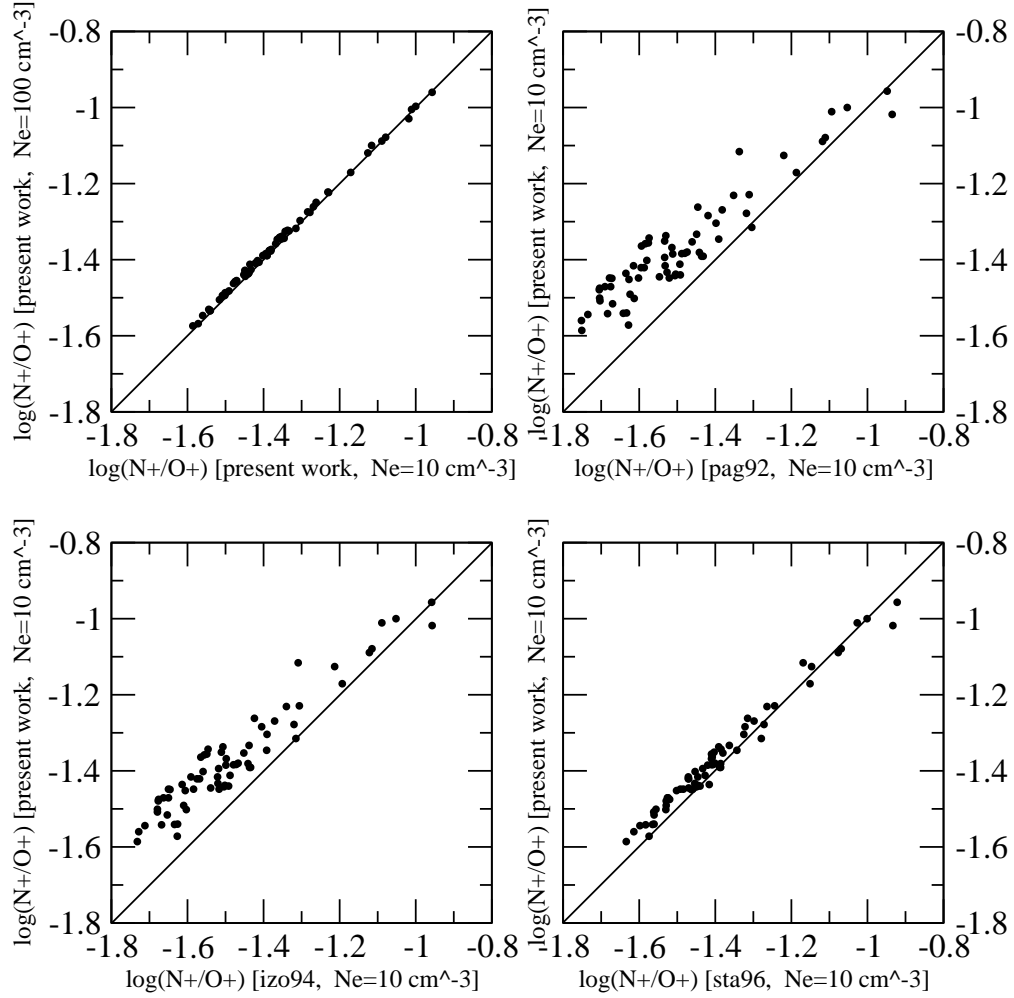


Fig. 7.— Comparison of  $\log(N^+/O^+)$  values derived for our sample objects using various parameterizations. The top-left panel is a plot of values obtained using Eqs. [10] & [11] (vertical axis) vs. values obtained using Eqs. [8] & [9] (horizontal axis). In the remaining panels values obtained using Eqs. [8] & [9] (vertical axis) are plotted against values obtained using pag92, izo94, or sta96, adopting  $N_e = 10 \text{ cm}^{-3}$ .



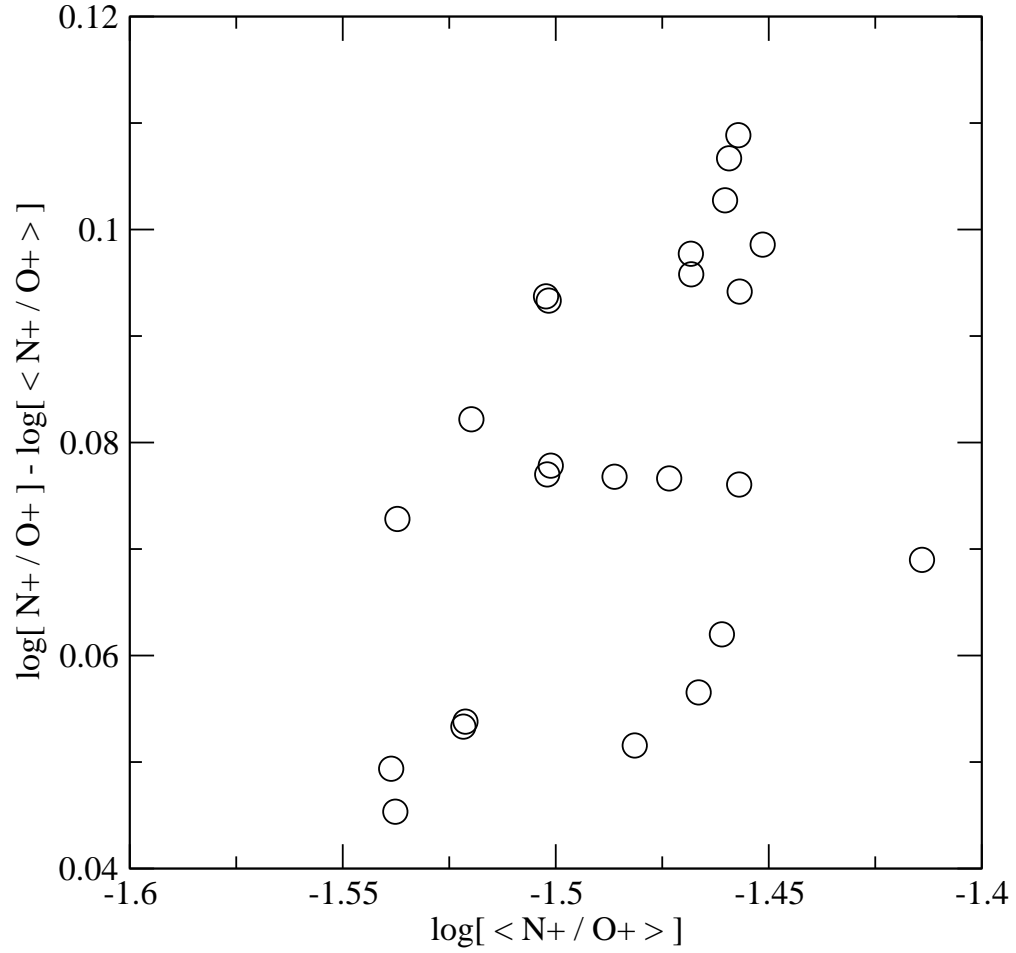


Fig. 8.— Difference  $\log[ N^+ / O^+ ] - \log[ \langle N^+ / O^+ \rangle ]$  as a function of  $\log[ \langle N^+ / O^+ \rangle ]$  for our CLOUDY models, where  $\log[ N^+ / O^+ ]$  is based on line flux ratios while  $\log[ \langle N^+ / O^+ \rangle ]$  is based on eq. [12].

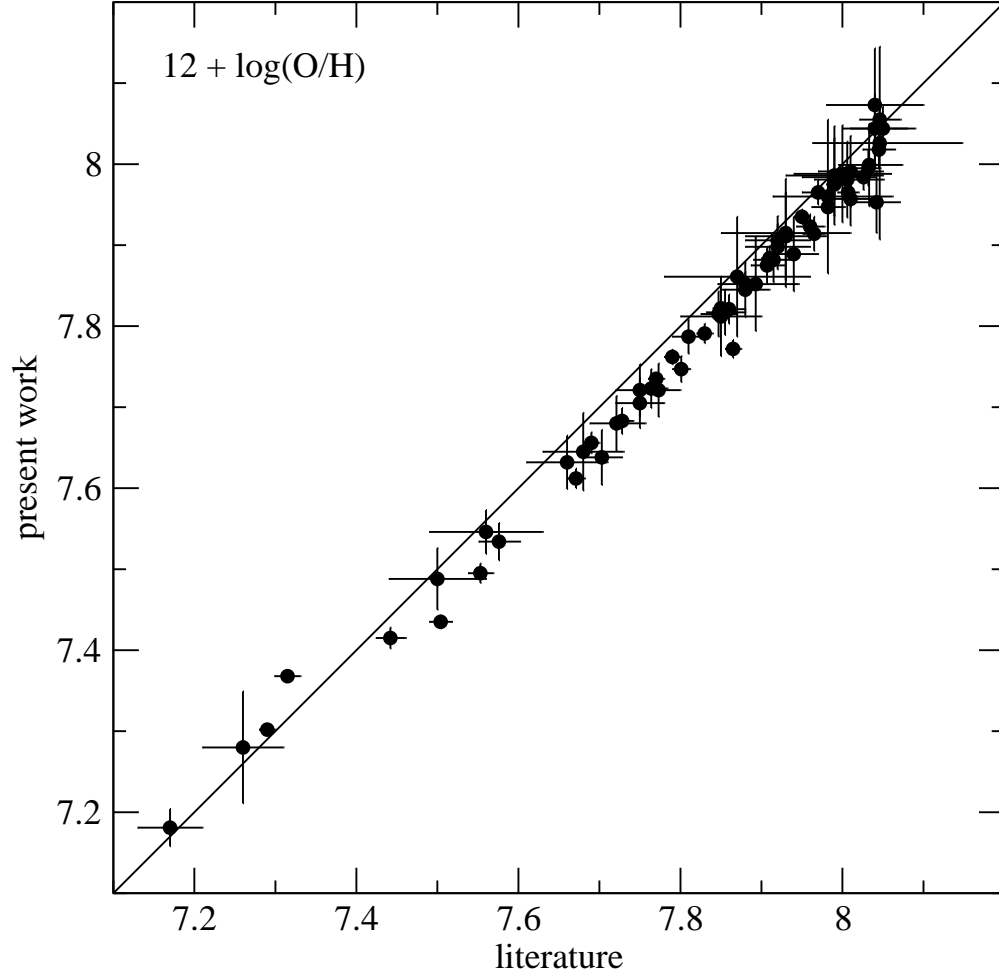


Fig. 9.— Present work vs. published  $12 + \log(\text{O}/\text{H})$  values for our sample of 68 low metallicity systems. The literature values were taken from the sources indicated in the footnote of Table 6. The diagonal represents points of one to one correspondance.

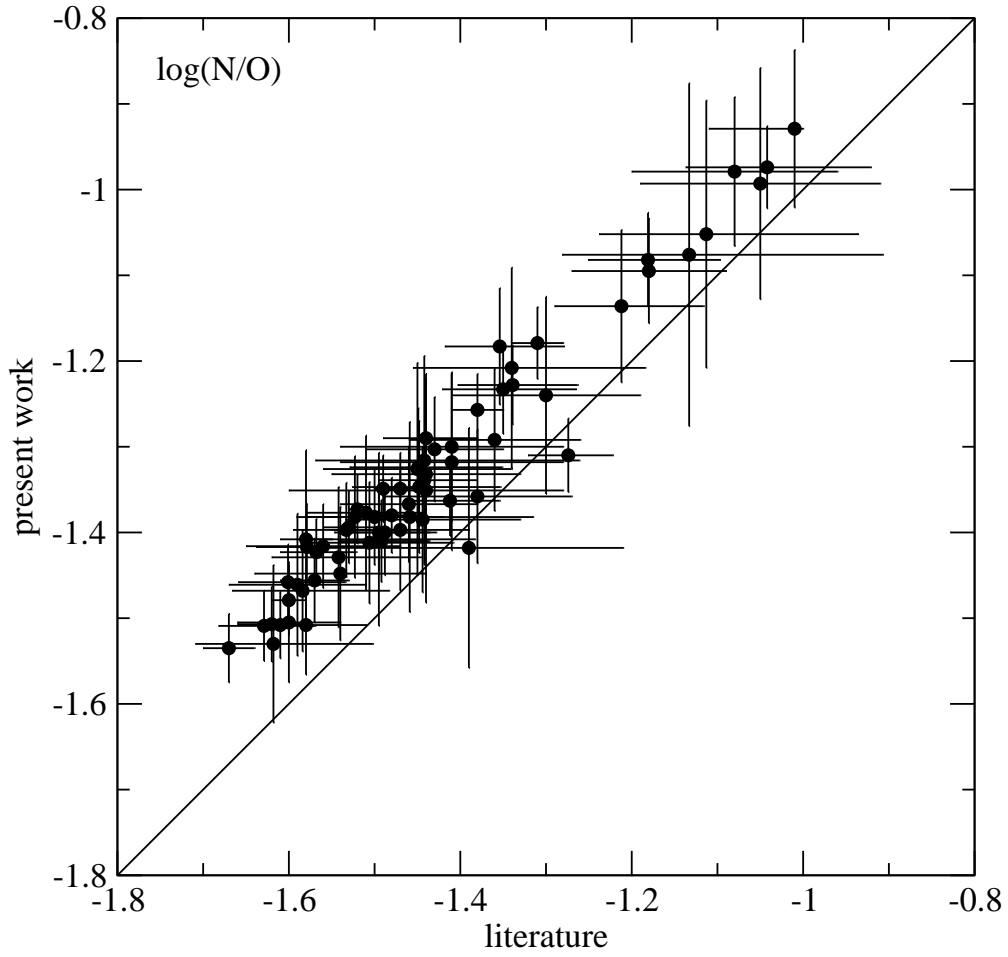


Fig. 10.— Same as Fig. 9 but for  $\log(N/O)$ .

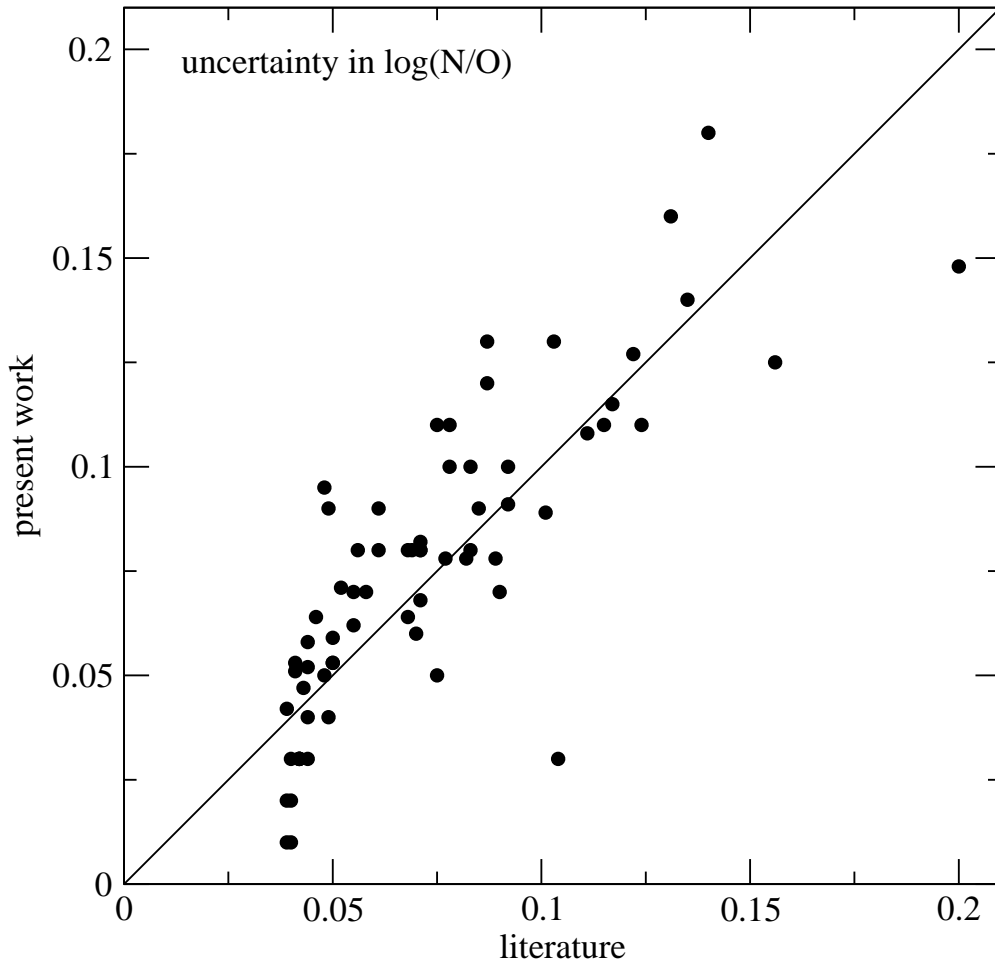


Fig. 11.— Same as Fig. 9 but for the uncertainty in  $\log(N/O)$ .

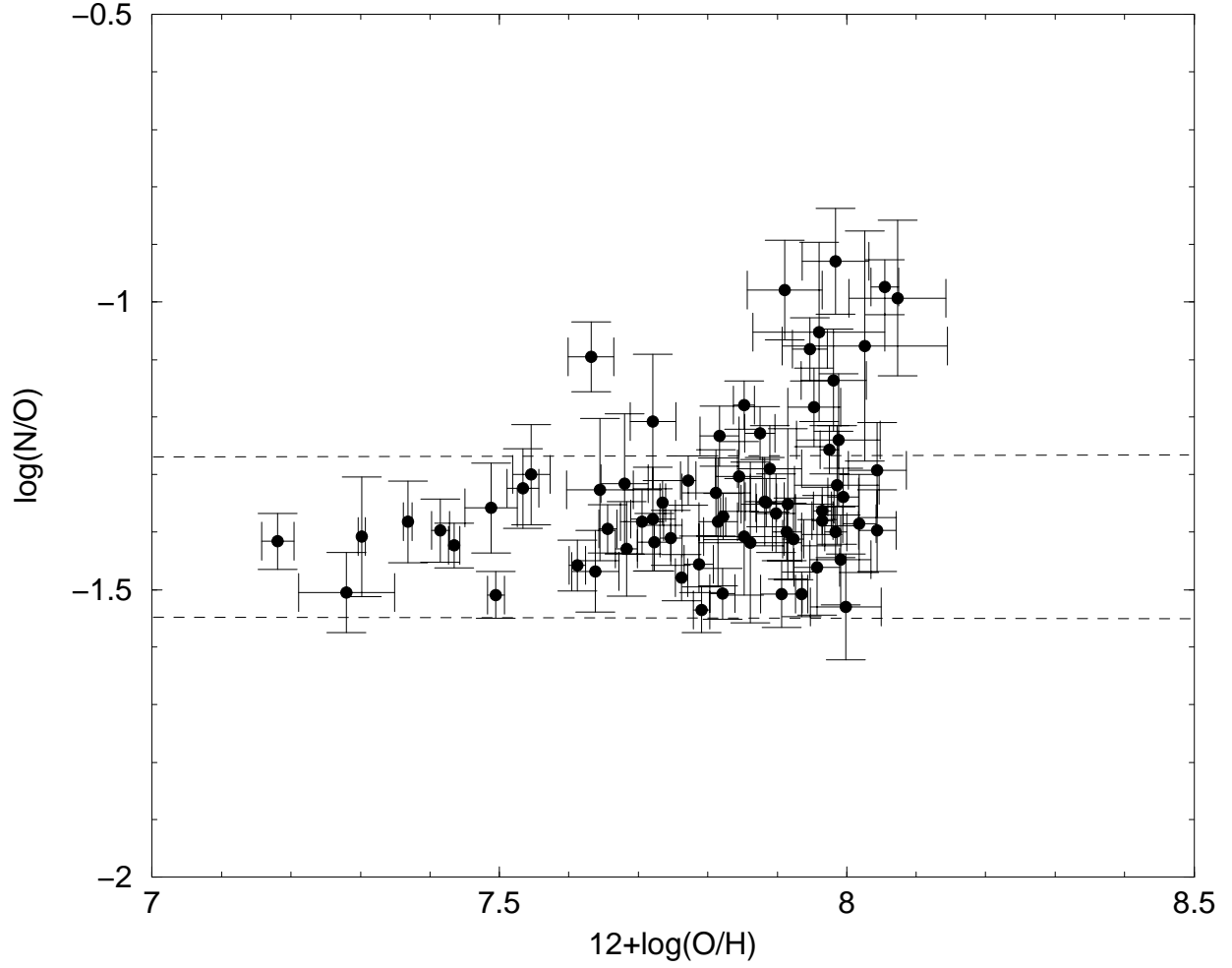


Fig. 12.—  $\log(\text{N/O})$  versus  $12 + \log(\text{O/H})$  as determined in this study for our sample objects. The dashed lines show the upper and lower limits for the N/O plateau as we define them (see the discussion of Fig. 13).

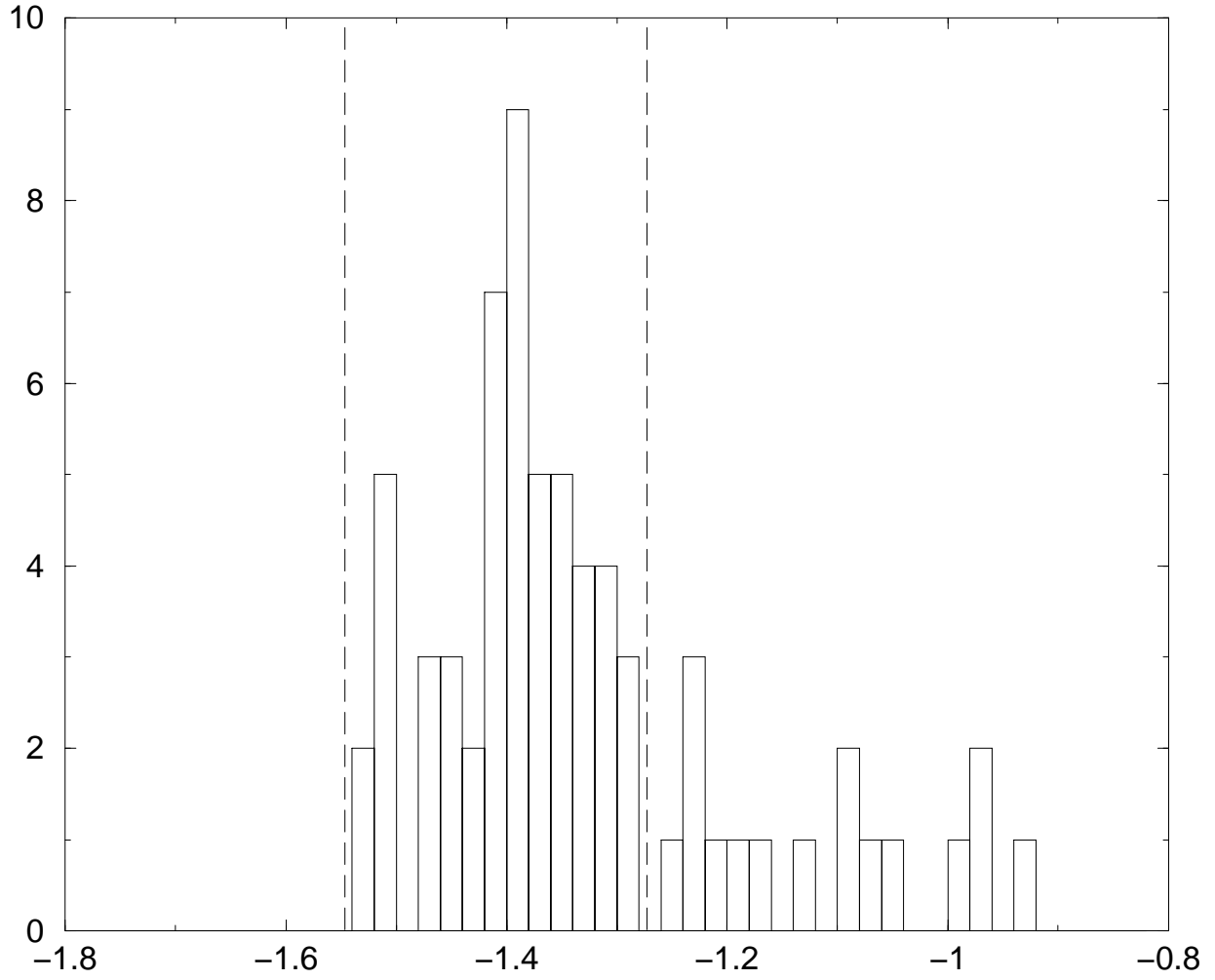


Fig. 13.— Observed distribution of values of  $\log(N/O)$  as determined in this paper. The vertical dashed lines show the upper and lower limits for the N/O plateau.